mBio (Research Article)

Chained structure of dimeric F_1-like ATPase in *Mycoplasma mobile* gliding machinery

Takuma Toyonaga[a], Takayuki Kato[b], Akihiro Kawamoto[b], Noriyuki Kodera[c], Tasuku Hamaguchi[a,d], Yuhei O Tahara[a,d], Toshio Ando[c], Keiichi Namba[e,f,g], Makoto Miyata[a,d,#]

[a]Graduate School of Science, Osaka City University, 3-3-138 Sugimoto, Sumiyoshi-ku, Osaka 558-8585, Japan.

[b]Institute for Protein Research, Osaka University, 3-2 Yamadaoka, Suita, Osaka, 565-0871, Japan.

[c]Nano Life Science Institute (WPI-NanoLSI), Kanazawa University, Kakuma-chou, Kanazawa, Ishikawa 920-1192, Japan.

[d]The OCU Advanced Research Institute for Natural Science and Technology (OCARINA), Osaka City University, 3-3-138 Sugimoto, Sumiyoshi-ku, Osaka 558-8585, Japan.

[e]Graduate School of Frontier Biosciences, Osaka University, 1-3 Yamadaoka, Suita, Osaka, 565-0871, Japan.

[f]RIKEN Center for Biosystems Dynamics Research and SPring-8 Center, 1-3 Yamadaoka, Suita, Osaka, 565-0871, Japan.

[g]JEOL YOKOGUSHI Research Alliance Laboratories, Osaka University, 1-3 Yamadaoka, Suita, Osaka, 565-0871, Japan.

[#]Address correspondence to Makoto Miyata, miyata@osaka-cu.ac.jp

Present address: Tasuku Hamagichi: Biostructural Mechanism Laboratory, RIKEN SPring-8 Center, 1-1-1 Kouto, Sayo, Hyogo, 679-5148, Japan.

Running title: Gliding machinery of *Mycoplasma mobile*

Keywords: F_1-ATPase, rotary motor, parasitic bacteria, electron microscopy, atomic force microscopy, bacterial motility

ABSTRACT

Mycoplasma mobile, a fish pathogen, exhibits gliding motility using ATP hydrolysis on solid surfaces, including animal cells. The gliding machinery can be divided into surface and internal structures. Interestingly, the internal structure of the probable gliding motor has 28 protein chains, each of which has 17 particles composed of homologs of the catalytic α- and β-subunits of F_1-ATPase. In this study, we isolated chain particles and determined their structures using negative-staining electron microscopy and high-speed atomic force microscopy. The isolated chain particles were composed of five proteins, MMOBs 1660 (α-subunit homolog), 1670 (β-subunit homolog), 1630, 1620, and 4530, and showed ATP hydrolyzing activity. The 2D structure, with dimensions of 35 and 26 nm, showed a hexameric ring dimer about 12 nm in diameter, resembling F_1-ATPase catalytic $(\alpha\beta)_3$. We isolated the F_1-like ATPase unit, which is composed of MMOBs 1660, 1670, and 1630. Furthermore, we isolated the complex in chain form and analyzed the 3D structure, showing that dimers of mushroom-like structures resembling F_1-ATPase were connected and aligned along the dimer axis at 31 nm intervals. An atomic model of F_1-ATPase catalytic $(\alpha\beta)_3$ from *Bacillus* PS3 was successfully fitted to each hexameric ring of the mushroom-like structure. These results suggest that the motor for *M. mobile* gliding shares an evolutionary origin with F_1-ATPase. Based on the obtained structure, we propose possible force transmission processes in the gliding mechanism.

IMPORTANCE

F_1F_o- ATPase, a rotary ATPase, is widespread in the membranes of mitochondria, chloroplasts, and bacteria, and converts ATP energy with a proton motive force across the membrane by its physical rotation. Homologous protein complexes play roles in ion and protein transport. *Mycoplasma mobile*, a pathogenic bacterium, was recently suggested to have a special motility system evolutionarily derived from F_1-ATPase. The present study isolated the protein complex from *Mycoplasma* cells and supported this conclusion by clarifying the detailed structures containing common and novel features as F_1-ATPase relatives.

INTRODUCTION

Mycoplasmas are parasitic bacteria characterized by small cell size, a short genome and lack of a peptidoglycan layer (1-3). Many *Mycoplasma* species exhibit a unique gliding motility, which is necessary for their infection (4-6). *Mycoplasma mobile* glides on solid surfaces at 2.0 to 4.5 μm/s in the direction of a protrusion on one side of the cell (Fig. 1A) (5). The gliding machinery is localized to the cell protrusion and can be divided into surface and internal structures (Fig. 1B, upper). The surface structure has approximately 450 repeats of a complex of three large proteins, Gli123, Gli521, and Gli349, inserted into the cell membrane (Fig. 1B, lower) (7-11). Fifty-nm-long leg structures corresponding to Gli349 molecules can be seen jutting out from cell protrusion by electron microscopy (EM) (12). The tip of Gli349 is characterized by a "foot" with an oval structure that can bind to sialylated oligosaccharides (SOs) (13-20). Gli521 and Gli123 serve as the "crank" that transfers force to Gli349 and the "mount" that localizes the other two surface proteins to the gliding machinery, respectively. A working model of the gliding mechanism has been proposed in which the cells are propelled by Gli349 molecules that repeatedly catch, pull, and release SOs on solid surfaces (5, 21-23).

The internal structure consists of a lumpy structure at the tip of the cell protrusion and 28 “chains” lining the inner membrane surface (Fig. 1B) (23-26). Each chain is characterized by 17 repeating particle structures, resulting in a total of 476 particles in one cell. The internal structure consists of least ten proteins (Fig. 1C). Six of these proteins, MMOBs 1620, 1630, 1640, 1650, 1660 and 1670 were

coded tandemly in a locus. Interestingly, MMOBs 1660 and 1670, which have Walker A and B motifs that are involved in ATP binding and hydrolysis (27), show high amino acid sequence identity with the catalytic subunits α and β of F_1-ATPase, respectively. MMOB1670 has an extra N-terminal region (amino acids 1–299), which is not present in the β subunit.

F_1F_o-ATPases, found in most organisms, are rotary motors that perform biological energy conversion (28, 29). Their role is to both synthesize ATP using a proton motive force and, conversely, to hydrolyze ATP to drive protons to maintain the membrane potential. Their structure is composed of a soluble catalytic F_1-domain for ATP catalysis and a membrane-embedded F_o-domain for the proton pathway. In the F_1-domain, the catalytic subunits α and β alternate to form a hexameric ring $(\alpha\beta)_3$ that rotates the central stalk penetrating the ring using ATP hydrolysis. Phylogenetic studies have shown that *Mycoplasma* have three F_1-like ATPase clusters, which are referred to as Type 1–3 ATPases (26, 30). Type 1, found in all mycoplasmas, is a typical operon encoding F_1F_o-ATPase and is likely to function as a proton pump to maintain membrane potential. Type 3 is found in mycoplasmas that have an MIB-MIP system to cleave host immunoglobulins (31). Type 2 is only found in four *Mycoplasma* species, including *M. mobile*. Interestingly, the Type 2 ATPase of *M. mobile*, which encodes MMOB1620–70, is involved in the internal structure of the gliding machinery.

Recently, the chains of the internal structure were shown to have structural changes linked to ATP hydrolysis, suggesting that they drive gliding motility (23, 32).

However, it is still unclear how the chain generates and transmits the force to the outside, because its detailed structure has not been clarified. In this study, we isolated the chains and their component particles and elucidated their structures. The structure had a common architecture with F_1-ATPase, suggesting that the chain shares a common evolutionary origin with F_1-ATPase. Based on our findings, we suggest two possible force transmission models for the gliding machinery.

Results

Isolation and biochemical analyses of chain particles. To examine the solubility of the chain particles, we lysed cultured *M. mobile* cells with 1% Triton X-100 and recovered the insoluble fraction by centrifugation (24). We then suspended the insoluble fraction with buffers containing various concentrations of NaCl and examined the solubility of the chain particles by centrifugation (Fig. S1). Approximately ten proteins were solubilized in NaCl at concentrations of 137 mM and higher, including MMOB1670, which is known to be a component of the chain (24). Based on this observation, we isolated the chain particles from *M. mobile* cells as follows: We suspended the Triton-insoluble fraction of *M. mobile* cells in a buffer containing 137 mM NaCl to solubilize the chain particles free of contaminating proteins. The soluble fraction recovered by centrifugation was then subjected to Superdex 200 gel filtration chromatography. The peak fraction in the void contained MMOBs 1620, 1630, 1660, and 1670, which are coded on the mycoplasma Type 2

ATPase operon, and MMOB4530 annotated as phosphoglycerate kinase (PGK) (Fig. 2A). These proteins are known to be components of the internal structure (Fig. 1C) (23-26). To examine the assembly of these proteins, we applied the isolated fraction to gel filtration chromatography using a Sephacryl S-400 HR column, which can fractionate up to 8000 kDa globular proteins (Fig. 2B). The proteins eluted as a single peak at a non-void position and were larger than 669 kDa, suggesting that they form a large complex. The molar ratios of the components were estimated to be 3.2:2.9:3.0:1.0:2.3 for MMOBs 1670, 4530, 1660, 1630, and 1620, respectively, from the relative intensity of the SDS-PAGE bands stained by Coomassie brilliant blue (CBB). We then analyzed the isolated fraction by blue-native (BN) PAGE (Fig. 2C, left). A single band was detected at approximately 1000 kDa, which is consistent with the gel filtration chromatography results. Next, we applied the band to an In-gel ATPase activity assay, which detects the activity as a white precipitation of lead caused by released of inorganic phosphate (Fig. 2C, right). The band with the complex showed precipitation, indicating ATPase activity. In addition, we assayed the isolated fraction for phosphate release from solution. The complex hydrolyzed ATP at a maximum turnover rate of 0.18 molecules/s per MMOB1670 subunit, β-subunit paralog with a K_m of 74 μM at 25°C (Fig. 2D). The ATPase activity was inhibited by addition of 15.4 mM sodium azide, an inhibitor to ATPases with Walker A motifs (33), with a K_m of 108 μM and a maximum turnover rate of 0.055 molecules/s. In a previous study, the Triton-insoluble fraction, which included the internal structure, showed ATPase activity with a K_m of 66 μM and a maximum

turnover rate of 0.09 molecules/s and was suppressed by 15.4 mM sodium azide, showing a K_m of 84 μM and a maximum rate of 0.063 molecules/s (23). The values obtained here are comparable to these previous data. The above results suggest that the chain particle is the motor in the internal structure of the gliding machinery.

Hexamers resembling F_1-ATPase catalytic $(\alpha\beta)_3$ form a dimer. We observed the isolated chain particles by EM using the negative-staining method. A field image showed uniform particles with axes of 20 and 40 nm (Fig. 3A and B). As the particle frequency depended on the protein concentration, we concluded that the observed particles were a part of the protein complex. We picked 2148 particle images automatically using RELION software (34) for 2D-classification. From the 2D-classification in 100 classes, we obtained four clear particle images (Fig. S2). We adopted mirror images according to the structure observed in high-speed atomic force microscopy (HS-AFM) (see below). Structural handedness cannot be judged from EM images because they are projections of electrons transmitted through the sample. We focused on an image showing a complex structure with dimensions of 35 and 26 nm featuring nearly two-fold symmetry (Fig. 3C and D). Interestingly, the characteristic hexamer of about 12 nm in diameter formed a dimer and was reminiscent of F_1-ATPase catalytic $(\alpha\beta)_3$. Considering that the amino acid sequences of MMOBs 1660 and 1670 have high identity to the α- and β-subunits of F_1-ATPase, respectively, the dimeric complex is probably evolutionarily related F_1-ATPase. The distance between the centers of the two hexamers was 11.0 nm. The complex had ten filamentous structures around the two hexamers, four of which

appeared to form bridges across the two hexamers. Hereafter, we refer to this structural unit as the “motor.”

The hexamer featured a ring and a peak. Next, we visualized the motor using HS-AFM to clarify the structure under liquid conditions. HS-AFM is a powerful method that can visualize the structure and dynamics of single molecules in liquid conditions at a video rate (35, 36). In this method, a specimen is placed on the stage surface and with a probe is scanned in buffer at high speed. In this study, we placed the isolated motor on a mica surface and scanned it in an area of 70 × 70 nm^2 at 56 × 56 pixels with a scanning rate of 100 ms per frame. HS-AFM images showed a complex with dimensions of approximately 30 and 20 nm composed of two globules and attached by 2–4 lateral protrusions shorter than 15 nm (Fig. 3E; Movie S1 and S2). The molecular images were categorized into two patterns as either a ring (pattern I) or a peak (pattern II), based on the central part. Then, we observed them at a higher resolution (area, 40 × 40 nm^2 with 50 × 50 pixels; scanning rate, 100 ms per frame) (Fig. 3F). In pattern I, the slice image near the top end of the motor between 9.8 and 11.3 nm above the substrate surface showed two hexameric rings (Fig. 3G). The position and direction of the two rings in the dimer are consistent with those of the hexamers in the negative-staining EM image. In addition, the distance between the centers of the two hexameric rings was 10.4 nm (Fig. 3H), in agreement with the distance between the centers of the hexamers in the negative-staining EM image (Fig. 3C). These observations suggest that the shape of the motor structure in liquid is preserved in negative-staining EM

conditions and that the hexamers form rings like F_1-ATPase catalytic $(\alpha\beta)_3$. In pattern II, the two central peaks were positioned 11.2 nm apart (Fig. 3H, lower), similar to the distance between the centers of the hexameric rings in pattern I (Fig. 3H, upper), suggesting that patterns I and II are two sides of the same coin (Fig. 3E, left). Interestingly, in most of the particles, the two peaks at 6 and 5 nm became invisible in 20 s, between frames 1 and 3 (Fig. 3I and J; Movie S3). We concluded that these subunits dropped out because they did not reappear until the complex was disrupted. Next, we focused on the lateral protrusions of these particles. To visualize them more clearly, we scanned the motor by HS-AFM with an area of 120 × 120 nm^2, 120 × 120 pixels, and scanning rate 500 ms per frame. The motor showed seven lateral protrusions around the two globules (Fig. 3K). These protrusions swayed without being fixed (Fig. 3L; Movie S4).

Isolation of F_1-like ATPase unit. Next, we treated the isolated motors with 1.5% sodium cholate, an anionic detergent. BN-PAGE and In-gel ATPase activity assays showed a single band with ATPase activity at a position lower than the original one, corresponding to 720–1048 kDa, indicating that the motor dissociated into smaller units with ATPase activity (Fig. 4A). To isolate the ATPase unit, we applied the motor treated with 1.5% sodium cholate to Sephacryl S-400HR gel filtration chromatography. The elution pattern showed at least five continuous peaks with broad peaks (Fig. 4B). The three peaks at elution volume 80–100 mL were 2–4 times larger than those of the other two peaks. These large peaks are thought to be formed by more than 20 different proteins, as shown by the reverse-stained

SDS-PAGE gel (Fig. S3). These proteins are probably rich in tryptophan and tyrosine residues because the absorbance at 280 nm wavelength was monitored during gel filtration. A CBB-stained SDS-PAGE gel showed that MMOBs 1670, 1660, and 1630 eluted in the same fractions, while MMOBs 4530 and 1620 eluted at later fractions (Fig. 4C), indicating that MMOBs 4530 and 1620 were dissociated from the motor by sodium cholate treatment.

We focused on the F6 fraction, which mainly contained MMOBs 1670, 1660, and 1630 (Fig. 4D). This complex corresponds to the BN-PAGE band showing ATPase activity (Fig. 4A), because only MMOBs 1660 and 1670 have the Walker A and Walker B motifs in the motor components. EM observation using the negative-staining method showed uniform globular particles 10–15 nm in diameter (Fig. 4EF). As the particle frequency depended on the protein concentration, we concluded that the observed particles were a part of the protein complex. We picked 11687 particle images automatically using RELION software for 2D-classification. By 2D-classifing the images in 50 classes, we obtained 15 clear particle images, which were averaged (Fig. S4). Fig. 4G shows a 12 nm diameter globule characterized by a single hexameric ring, corresponding to a part of the motor image in Fig. 3C. Three of the subunits were larger than the others with hook structures on either side of the edge. Three averaged images (II–IV) showed a mushroom-like structure resembling F_1-ATPase, which is characterized by a 12 nm-diameter umbrella and a 3 nm-long stalk (Fig. 4G). These observations suggest that MMOBs 1670, 1660, and 1630 form an F_1-like ATPase unit. MMOB4530 was

probably not included in this unit because it probably binds to the complex and could not be distinguished in the image due to the low proportion of bound entities (Fig. 4D). Thus, the hexameric ring is likely formed by the α-subunit homolog MMOB1660 and the β-subunit homolog MMOB1670, and the stalk is formed by MMOB1630.

Motor chain structure. In gliding machinery, motors link to form chains. To isolate the chain, 387 mM NaCl was added to the Triton-insoluble fraction from *M. mobile* cells. We then applied this fraction to gentle mixing and centrifugation at 5000 × *g* for 5 min, milder conditions than that for motor (chain particle) isolation. The supernatant contained more than 20 proteins, including the motor component proteins MMOBs 1670, 4530, 1660, 1630, and 1620 as major components (Fig. 5A). EM observation using the negative-staining method showed chain structures with lengths longer than 70 nm and particles of various sizes (Fig. 5B and C). This time we manually picked 2127 particles from the chain images using RELION software, overlapping approximately 50% of the 71 × 71 nm^2 box area. From 2D-classifcation in 20 classes, we obtained seven clear particle images (Fig. 5D). The particle images show the various orientations required for 3D reconstruction. We then created a 3D map by combining a total of 1709 particle images of good quality (Fig. 5E and S5). The 3D map with dimensions of 70, 20, and 15 nm at a density threshold (contour level = 0.026) was composed of two dimers of mushroom-like structures resembling F_1-ATPase, aligned along the dimer axis (Fig. 5E). The dimers were connected by a bulge structure with a diameter of 5 nm. The chain

interval was 31 nm, consistent with the corresponding dimension in a 2D image from electron cryotomography (ECT) (23), suggesting that the 3D model obtained reflects the original structure from a cell. The mushroom-like structure with a diameter of 15 nm, consisting of a hexameric ring and a central stalk, was connected to the dimer by two bridge structures with a diameter of 3–6 nm. An atomic model of F_1-ATPase catalytic $(\alpha\beta)_3$ from *Bacillus* PS3 (PDB ID 6N2Y) (37) was fitted into each hexameric ring of the mushroom-like structure (Fig. 5F). The distance between the centers of the fitted $(\alpha\beta)_3$ in the dimer was 12.5 nm, which is in agreement with that of the motor observed by negative-staining EM and HS-AFM (Fig. 3C and H). The fitted model showed that each hexameric ring had two protrusions of 3–6 nm pointing laterally (Fig. 5F). The cross-sections of each mushroom-like structure showed the central stalk length of 5 nm (Fig. 5G). A cavity was observed at the center of the hexameric ring. However, it may be an artifact of the low-resolution map of negative-staining EM, because metal coating tends to emphasize the peripheral part of large particles (38). Next, we compared a reprojection image of the 3D chain map with the 2D averaged image of the motor from negative-staining EM (Fig. 5H). Two short filaments marked by asterisks in the dimer (Fig. 5H, left) are positioned facing each other in the connecting bulge (Fig. 5H). Previously, electron cryotomography (ECT) of a permeabilized *M. mobile* cell showed a chain structure characterized by repeats of two globules and two types of projections to the cell membrane (Fig. 5I, left) (23). The hexameric ring and the central stalk in the 3D map here correspond to the globule and one type of

projection to the cell membrane in the ECT image, respectively, suggesting that the chain is oriented with the central stalk facing the membrane, which is common in F_1-ATPases. At the interface between the motors, the 3D map here did not include a structure composed of another type of projection and a globule as observed in the ECT image. The subunits corresponding to these structures probably had structural variations or dissociation during the isolation process.

Discussion

Outline of internal structure of gliding machinery. Previously, sequence analysis suggested that the chain of *M. mobile* gliding machinery evolved from F_1-ATPase (5, 23-26). The present study supports this conclusion by structural data showing that the chain has hexameric rings similar to the F_1-ATPase catalytic $(\alpha\beta)_3$. Integrating available information, we can now describe the outline of the internal structure of *the M. mobile* gliding machinery (Fig. 1B). *M. mobile* cells have 28 individual 530 nm long chains, each of which contains 17 motor units composed of two F_1-like ATPases and filamentous structures (23). The central stalk of the F_1-like ATPase and another protrusion from the connecting bulge project to the cell membrane.

Unique role of F_1-ATPase related complex. To date, several complexes are known to be evolutionarily related to F_1-ATPase, all of which are responsible for transporting substances across the membrane (39). However, the motor we

303 identified here most likely plays a role in motility. This case may be reminiscent of
304 dynein, a motor in eukaryotes, which evolved from a widely conserved AAA
305 (ATPases associated with diverse cellular activities)+ protein, in which multiple
306 subunits of ATPases perform functional rotation (40, 41). Sequence analyses have
307 shown that mycoplasma Type 3 ATPase is also related to F_1-ATPase, and its role
308 has been suggested to promote substrate turnover in the MIB-MIP system (31). If
309 Type 3 ATPase provides the force to change the conformation of a hydrolytic
310 enzyme, its role in force generation is common with Type 2, the gliding motor.
311 F_1F_o-ATPases are known to be dimerized through interactions between
312 F_o-domains and are usually arranged in rows along the short axis in the tightly
313 curved cristae ridges of mitochondria (29, 42, 43). The dimer structure found in the
314 present study is not related to this, because the F_1-like domain is dimerized through
315 the filament structure and is linked in the long axis direction. However, some roles
316 may be common in part if the dimerization and chain formation observed in the
317 gliding motor identified in this study stabilizes the membrane structure, as seen in
318 the F_1F_o-ATPase dimer (44). Moreover, dimerization may result in cooperativity in
319 motor functions. The gliding motor here is mostly a two-rotational symmetrical
320 structure, whereas gliding occurs unidirectionally. The directionality may be
321 provided by the surface part of the gliding machinery rather than the gliding motor
322 itself. In fact, the binding of cells to sialic acids is known to have directionality, which
323 is probably provided by the foot of Gli349 (14, 16, 45).
324 **Protein assignment.** The α-subunit homolog MMOB1660 (58.7 kDa) and the

β-subunit homolog MMOB1670 (88.4 kDa) likely correspond to the smaller and larger subunits, respectively, of the hexameric ring of an F_1-like ATPase unit, as suggested by the estimated 1:1 molar ratio in the motor (Fig. 2B). This means that the hook structure of the larger subunit may be formed by the extra N-terminal region (34.8 kDa) of MMOB1670. Previously, 3D structure modeling based on secondary structure suggested that MMOB1630 is structurally similar to the γ subunit, the principal component of the central stalk of F_1-ATPase (5). In general, the γ subunit of F_1-ATPase is composed of a coiled-coil and a globular domain and penetrates the hexameric ring (46). In the F_1-like ATPase unit and chain 3D model, a stalk structure, suggesting the globular domain of the γ subunit, was found in the center of the hexameric ring (Fig. 4G and 5G), implying that MMOB1630 penetrates the hexameric ring like the γ subunit.

Using HS-AFM observations, the peak at approximately 5 nm at the center of the hexameric ring dropped out with time (Fig. 3I). The peak height agrees with the length of the estimated globular domain of MMOB1630 in the chain 3D model (Fig. 3J and 5G), suggesting that the peak is composed of MMOB1630 and was pulled out from the hexameric ring by the scanning cantilever during HS-AFM observation. The pull-out event is thought to be common to that of the F_1-ATPase, in which the γ subunit is removed from the hexameric ring by optical tweezers (47).The filamentous structures around the hexameric ring probably correspond to lateral protrusions in the HS-AFM images and are formed by the remaining proteins, MMOB1620 and MMOB4530 (PGK). These proteins probably play roles in ATPase

dimerization, chain formation, and chain bundling (23). MMOB1620 is an unannotated protein specific to the Type 2 ATPase cluster (26, 30). MMOB4530 is annotated as an enzyme that transfers phosphate groups from 1,3-bisphosphoglycerate to ADP in glycolysis to yield ATP and 3-phosphoglycerate (48). In *M. mobile*, ATP is probably provided by glycolysis (49). MMOB4530 may supply ATP efficiently to the gliding motor by its close proximity. Yeast V-ATPase, which belongs to the rotary ATPase family like F_1F_o-ATPase, is also attached by two glycolytic enzymes, 6-phosphofructo-1-kinase and aldolase (50-52). These glycolytic enzymes are involved in the regulation of V-ATPase assembly and activity.

Possible force transmission mechanisms for gliding. The involvement of an internal ATPase in the gliding mechanism is based on the following five observations from the analysis of the "gliding head" of *M. mobile* protrusions and of the isolated gliding machinery: (a) The affinity for ATP is comparable in the ATPase activity of the internal structure and the speed of the gliding head (23). (b) Substrate binding and gliding speed of the gliding head are inhibited by azide, as well as the ATPase activity of the internal structure (23). (c) The chain in the internal structure undergoes conformational changes based on ATP hydrolysis (23, 32). (d) Among the 21 proteins identified from the gliding head, only MMOBs 1660 and 1670 could be suggested for ATPase from the amino acid sequences alone (23, 24). (e) Fluorescent protein tagging of components of the internal structure significantly affects the binding activity and gliding speed of *M. mobile* cells (26).

The structure elucidated in the present study allows us to discuss the gliding mechanism in more detail. In F_1-ATPase, the three catalytic sites in the hexameric ring cooperatively hydrolyze ATP, and each catalytic β-subunit undergoes a bending motion that drives the rotation of the central stalk (46). Previously, structural changes linked to ATP hydrolysis were reported: (I) EM studies showed 2 nm contraction of particle intervals in the isolated chains (23), and (II) HS-AFM studies showed movements of individual motors in the cell 9 nm perpendicular to the chain long axis and 2 nm into the cell (32). Considering these observations, we propose two different working models for the force transmission mechanism in gliding (Fig. 6). In the “contraction model” (Fig. 6 i), the force generated by the hexameric ring shortens the chain. The resulting displacement of the projections from the motor to the cell membrane drives the hook structure of Gli521 like a "lever.” Then, the leg moves with the catch, pull, and release of the SOs. In the “rotation model” (Fig. 6 ii), the force generated by the hexameric ring rotates MMOB1630 in the same way as F_1-ATPase. This rotation is transmitted across the cell membrane to the Gli521. The hook structure converts rotational motion into linear motion of the leg, similar to a crank. Previous studies have reported that *M. mobile* exhibits unitary steps of approximately 70 nm in size at no load (53, 54). In our models, both the rotation and contraction displacements are expected to be a few nanometers. These displacements may be amplified by the large surface structure complex formed by the 100 nm long Gli349 and 120 nm long Gli521, which show dimensions comparable to the step size, acting as a large gear (22). This conjecture could

391 explain how a single leg exerts a force of 1.5 pN, smaller than that of conventional
392 motor proteins such as myosin, dynein, and kinesin.

393 **Evolution of *M. mobile* gliding.** A previous study suggested that Gli349 evolved
394 from a static binding receptor to parasitize the host (16). Considering this, the
395 evolutionary origin of *M. mobile* gliding can now be discussed. F_1F_o-ATPase, which
396 is abundant on the cell membrane, could have been accidentally associated with
397 the binding receptor and turned into a primitive motility system, which may have
398 provided random cell spreading. The system was then refined under survival
399 pressure, because motility might be beneficial to infection and evading the host's
400 immune system. For dimerization and chain formation, PGK was then incorporated
401 into the gliding machinery, because PGK was working in close proximity to
402 F_1F_o-ATPase.

403

404 **Materials and Methods**

405 **Strains and culture conditions.** We used P476R *gli521*, a mutant strain of *M.*
406 *mobile* that can glide normally but binds SOs more tightly than wild-type strains (10,
407 22, 55). *M. mobile* cells were cultured as described previously (56, 57).

408 **Optical microscopy.** The cultured cells were inserted into a tunnel chamber
409 assembled with two coverslips and double-sided tapes and observed by
410 phase-contrast microscopy using an inverted microscope (IX71; Olympus, Tokyo,
411 Japan) (17, 19). Movement was recorded using a complementary metal-oxide
412 semiconductor (CMOS) camera (DMK33UX174; The Imaging Source, Bremen,

413 Germany). Video was analyzed using the ImageJ software, version 1.53a
414 (http://rsb.info.nih.gov/ij/).

415 **Chain particle isolation.** All procedures were performed at 4°C unless
416 otherwise noted. To investigate the solubility of the chain particle, *M. mobile* cells
417 from 60 mL of culture medium were collected by centrifugation at 14000 × *g* for 20
418 min and washed twice with PBS consisting of 8.1 mM Na_2HPO_4, 1.5 mM KH_2PO_4,
419 pH 7.3, 2.7 mM KCl and 137 mM NaCl. Cells were resuspended in PBS to a 12-fold
420 higher concentration than the culture and sonicated for 1 min at 24–27°C to be
421 dispersed in microtubes using an ultrasonic generator (2510 J-MT; BRANSON,
422 Kanagawa, Japan). The cells were then treated with Triton solution (1% Triton
423 X-100, 0.1 mg/mL DNase, 5 mM $MgCl_2$, and 1 mM phenylmethylsulfonyl fluoride in
424 PBS) in a total volume of 10 mL. After gentle shaking for 30 min, the suspensions
425 were centrifuged at 20000 × *g* for 20 min, and pellets were collected and washed
426 once with suspension buffer, PBS with 5 mM $MgCl_2$. Pellets were then resuspended
427 in suspension buffer with 0 to 400 mM NaCl by pipetting several times. After
428 overnight treatment, suspensions were centrifuged at 20000 × *g* for 20 min, and
429 supernatants and pellets collected for SDS-PAGE analysis.

430 For isolation of chain particles, *M. mobile* cells from 1.2-liter cultures were
431 collected by centrifugation at 14000 × *g* for 30 min and washed three times with
432 PBS. The cells were resuspended in PBS to a 100-fold higher concentration than
433 the culture and sonicated for 1 min using an ultrasonic generator at 24–27°C. The
434 cells were treated with 0.05 mg/mL RNase in Triton solution in a total volume of 207

435 mL. After 1 h of gentle shaking, the suspension was centrifuged at 20000 × *g* for 20
436 min, and pellets were washed once with suspension buffer. Pellets were then
437 resuspended in suspension buffer by pipetting up and down and allowed to dissolve
438 overnight. The soluble fraction was collected by centrifugation at 20000 × *g* for 20
439 min and loaded onto a HiLoad 16/600 Superdex 200 column (Cytiva, Tokyo, Japan)
440 equilibrated with 1 mM $MgCl_2$ in PBS at a flow rate of 0.8 mL/min. The fractions
441 were analyzed by SDS-PAGE and CBB staining. Focused protein bands were
442 identified by PMF, as previously reported (24, 58), and the chain particle fraction
443 was recovered.

444 We modified this procedure to isolate the F_1-like ATPase unit. The washed *M.*
445 *mobile* cells were treated with Triton solution in a total volume of 207 mL. After 1 h
446 of gentle shaking, the suspension was centrifuged at 20000 × *g* for 20 min, and the
447 pellet was washed once with suspension buffer. The pellet was suspended in 20
448 mM Tris-HCl (pH 7.5), 250 mM NaCl, 1 mM phenylmethylsulfonyl fluoride, and 1
449 mM $MgCl_2$ with pipetting as before and allowed to dissolve overnight. The soluble
450 fraction was collected by centrifugation at 20000 × *g* for 20 min and mixed with 2%
451 (w/v) sodium cholate. After 7 h of incubation, the complexes were loaded onto a
452 Sephacryl S-400 HR column (Cytiva) equilibrated with 0.7% sodium cholate, 20 mM
453 Tris-HCl (pH 7.5), 250 mM NaCl, and 1 mM $MgCl_2$ at a flow rate of 0.5 mL/min. The
454 elution curve was fitted using Igor Pro 6.34j (WaveMetrics, Lake Oswego, OR, USA).
455 The fractions were analyzed by SDS-PAGE and CBB- and reverse-staining (59, 60).
456 The fraction of the complex composed of MMOBs 1670, 1660, and 1630 was

457 collected. Samples were concentrated using an Amicon Ultra 100 K spin filter
458 (Merck KGaA, Darmstadt, Germany), if necessary.

459 **Isolation of chain.** All procedures were performed at 4°C. *M. mobile* cells from
460 15 mL of culture medium were collected as a pellet by centrifugation at 14000 × *g*
461 for 25 min and washed twice with PBS. Cells were resuspended in PBS to a
462 100-fold higher concentration than the culture and sonicated for 1 min at 24–27°C in
463 microtubes using an ultrasonic generator. The cells were then treated with Triton
464 solution as above in a total volume of 300 µL. After gentle shaking for 30 min, the
465 suspension was centrifuged at 20000 × *g* for 20 min, and the pellet containing the
466 internal structures was resuspended in suspension buffer. The suspension was then
467 gently mixed with an equal volume 500 mM NaCl in suspension buffer. The chain
468 was recovered as the supernatant by centrifugation at 5000 × *g* for 5 min.

469 **Analytical gel filtration.** The isolated chain particle solution was loaded onto a
470 Sephacryl S-400 HR column equilibrated with gel filtration buffer containing 20 mM
471 Tris-HCl (pH 7.5), 200 mM NaCl and 1 mM $MgCl_2$ at a flow rate of 0.5 mL/min at 4°C.
472 Thyroglobulin (669 kDa; Gel Filtration Calibration Kits; Cytiva) was dissolved in gel
473 filtration buffer and loaded onto the column as a size standard at a flow rate of 0.5
474 mL/min. The stoichiometry of protein complexes was estimated by densitometry of
475 SDS-PAGE gels stained with CBB, using a scanner (GT-9800F; Epson, Nagano,
476 Japan) and ImageJ (9).

477 **BN-PAGE and in-gel ATPase activity assays** BN-PAGE was performed
478 according to the user manual of the Native PAGE Novex Bis-Tris Gel System

(Thermo Fisher Scientific, Waltham, MA). For BN-PAGE of the F_1-like ATPase unit, the isolated chain particle (motor) fraction was mixed with sodium cholate (1.5%) and incubated at 4°C for 9 h. When this sample was mixed with a sample buffer, NativePAGE™ 5% (w/v) G-250 sample additive was also added at 0.5% (w/v) to prevent protein aggregation. Thyroglobulin was dissolved in water and used as a negative control for the In-gel ATPase activity assay. For the In-gel ATPase activity assay (61, 62), native gels were incubated with gentle shaking overnight at 24–27°C in activity buffer containing 270 mM glycine, 35 mM Tris (pH 8.4), 4 mM ATP, 14 mM $MgSO_4$, and 0.2% (w/v) $Pb(NO_3)_2$. The gels were rinsed once with water and images were taken using ImageQuant LAS 4000 mini (Cytiva). White precipitates were then dissolved by gentle shaking overnight at 24–27°C with 50% (v/v) methanol and 10% (v/v) acetic acid in water. The gels were restained with 0.025% (w/v) CBB G-250 and 10% acetic acid in water for 80 min at 24–27°C with gentle shaking and destained with 10% (v/v) ethanol and 10% acetic acid in water for 180 min at 24–27°C with gentle shaking. The gels were rinsed once with water and images were taken using ImageQuant LAS 4000 mini.

Phosphate-release assay The isolated chain particle solution was dialyzed overnight using 20 mM Tris-HCl (pH 7.5), 150 mM NaCl, and 2 mM $MgCl_2$. ATPase activity was assayed by a continuous spectrophotometric method using a 2-amino-6-mercapto-7-methylpurine ribonucleoside–purine nucleoside phosphorylase reaction to detect released inorganic phosphate (EnzChek kit; Thermo Fisher Scientific) (63). The reaction mixture was as follows: 15.7 nM motor,

20 mM Tris-HCl (pH 7.5), 150 mM NaCl, 2 mM $MgCl_2$ and 0.01–1 mM ATP in a total volume of 0.2 mL at 25°C. Sodium azide was added to 15.4 mM final concentration when the reaction was started. The protein amount of the MMOB1670 comprising F_1-ATPase β-subunit paralogs was estimated using densitometric of SDS-PAGE.

Negative-staining EM and image processing. The isolated chain particle solution was placed on a glow-discharged (PIB-10; VACUUM DEVICE, Ibaraki, Japan) carbon-coated grid (F-400; Nisshin EM Co., Tokyo, Japan) and incubated for 1 min at 24–27°C. The solution was then removed, and the grid was stained with 2% uranyl acetate (w/v) for 30 s. The stain was then removed, and the grid was air-dried. To observe the F_1-like ATPase unit and the chain, the grids were washed with water after 1 min of incubation and then treated as described for the isolated chain particle solution. Samples were observed using a transmission EM (JEM1010, JEOL) at 80 kV, equipped with a FastScan-F214 (T) charge-coupled-device (CCD) camera (TVIPS, Gauting, Germany), and images were captured at 2.58 Å/pix.

The contrast transfer function parameters for electron micrographs were estimated using Gctf (64). Further image processing was performed using RELION 3.0 (34). A total of 2148 particles for the chain particle and 11687 particles for the F_1-like ATPase unit were automatically selected with box sizes of 180 × 180 and 100 × 100 pixels, respectively. These particle images were binned to 5.16 Å/pix. For the chain particle, the particle images were 2D-classified into 100 classes. For the F_1-like ATPase unit, particle images were 2D-classified in four rounds, and the selected 7381 particles were re-extracted with the pixel size returned to the

unbinned image and then 2D-classified into 50 classes.

For reconstruction of the 3D chain structure, 2127 particles were manually selected for chains with a box size of 276 × 276 pixels with ~50% overlap. These particle images were binned to 5.16 Å/pix. Particle images were 2D-classified in two rounds, and the selected 1709 particles were used to reconstruct the initial model with a final resolution limit of 50 Å. The initial model and selected particles were used to perform 3D refinement. Reprojection images were produced from the 3D map using the relion_project command in RELION. The 3D map was visualized using UCSF Chimera 1.14 (65). Atomic models of F_1-ATPase catalytic $(\alpha\beta)_3$ from *B. subtilis* (PDB ID 6N2Y) were fitted into the 3D map using command of "Fit in map" in UCSF Chimera.

HS-AFM. Imaging was performed with a laboratory-built tapping mode HS-AFM (66, 67), using small cantilevers (BLAC10DS-A2, Olympus; resonant frequency, ~0.5 MHz in water; quality factor, ~1.5 in water; spring constant, ~0.1 N/m). The cantilever's free-oscillation peak-to-peak amplitude (A_0) and set-point amplitude were set at ~2.5 nm and ~0.8 × A_0, respectively. The probe tip was grown on the original tip end of a cantilever through electron beam deposition and further sharpened using a radio frequency plasma etcher (PE-2000, South Bay Technology, Redondo Beach, CA) under an argon gas atmosphere (typically at 180 mTorr and 15 W for 3 min). The sample was deposited on a freshly cleaved mica disc glued to a glass stage beforehand. After 3.5 min, the stage surface was immersed in a liquid cell containing an observation buffer [20 mM Tris-HCl (pH 7.5), 50 mM KCl, 2 mM

545 $MgCl_2$]. Imaging was performed at 24–27°C. AFM images were processed using a
546 low-pass filter to remove spike noise and make the *xy*-plane flat and analyzed using
547 Kodec software (version 4.4.7.39) (68). Surface profiles and smoothing were
548 performed using ImageJ software.
549

550 Acknowledgments

551 We thank Toshiaki Arata, Ikuko Fujiwara, Kohei Kobayashi, and Hiroki Sato at the
552 Graduate School of Science, Osaka City University, and Takayuki Uchihashi at the
553 Department of Physics and Structural Biology Research Center, Nagoya University,
554 for helpful discussions. We also thank Aya Takamori at the Graduate School of
555 Science, Osaka City University, for performing MALDI-TOF MASS spectrometry. TT
556 learned RELION software in an instruction course on 20180927–28 provided by the
557 Cyclic Innovation for Clinical Empowerment (CiCLE) from AMED.
558 This work was supported by a Grant-in-Aid for Scientific Research on the Innovative
559 Area "Harmonized Supramolecular Motility Machinery and Its Diversity" (MEXT
560 KAKENHI Grant Number JP24117002), by a Grants-in-Aid for Scientific Research
561 (B) and (A) (MEXT KAKENHI Grant Numbers JP24390107, JP17H01544), by JST
562 CREST Grant Number JPMJCR19S5, Japan, by the Osaka City University (OCU)
563 Strategic Research Grant 2018 for top priority researches and by a Grant-in-aid of
564 the FUGAKU TRUST FOR MEDICINAL RESEARCH to MM, and JSPS KAKENHI
565 (Grant Number JP25000013), the Platform Project for Supporting Drug Discovery

and Life Science Research (BINDS) from AMED (Grant Number JP19am0101117 and support number 1282), CiCLE (Grant Number JP17pc0101020), and JEOL YOKOGUSHI Research Alliance Laboratories of Osaka University to KN.

Figure Legends

FIG 1. Gliding machinery of *Mycoplasma mobile*. (A) Optical microscopy of cells (upper) and trajectories of gliding cells (lower). The gliding direction is indicated by a black arrow. The 4-second trajectory is colored from red to blue. (B) Schematic illustration of gliding machinery based on the present study. In the whole cell shown in upper illustration, the internal structure and legs are colored gray and red, respectively. The actual cell has about 28 chains, each consisting of 17 particles, although a more limited number is illustrated here. A single unit of the surface structure and a chain of the internal structure are magnified in the lower illustration. “Motor” is identical to “chain particle.” (C) ORFs for the internal structure. The components of the internal structure are colored gray. Type 2 ATPase operon is at the top. Motor components revealed in the present study are marked by colored boxes, corresponding to the colored components of the lower illustration in panel B.

FIG 2. Isolation profile and characterization of chain particle. (A) Protein profile of each fraction. The fractions were subjected to SDS-12.5% PAGE gel and stained with CBB. Lane 1, lysate of *M. mobile* cells; lane 2, Triton-soluble fraction; lane 3, Triton-insoluble fraction; lane 4, supernatant after incubation in a buffer containing

588 137 mM NaCl; lane 5, peak fraction of Superdex 200 gel filtration chromatography.
589 The bands of the chain particle components are marked by black triangles.
590 Molecular masses are shown on the left. (B) Gel filtration assay using Sephacryl
591 S-400 HR column. The peak position of thyroglobulin (669 kDa) is marked by a
592 purple triangle. The peak fraction of the chain particles marked by an orange
593 triangle was analyzed by SDS-12.5% PAGE. The bands of the chain particle
594 components are marked by black triangles. (C) BN-PAGE (left) and In-gel ATPase
595 activity assay (right). Isolated chain particle and thyroglobulin, which has no ATPase
596 activity, were subjected to 3 to 12% gradient BN-PAGE. The band positions of the
597 chain particle and thyroglobulin are marked by black and open triangles,
598 respectively. White precipitates, indicating ATPase activity, appeared only at the
599 band position of the chain particle. Molecular masses are shown on the left. (D)
600 Phosphate release assay under various ATP concentrations with and without
601 sodium azide. The ATPase activities under 0- and 15.4-mM sodium azide are
602 marked by red and green filled circles, respectively (n = 3). These data were fitted
603 by the Michaelis-Menten equation as solid lines.
604
605 **FIG 3. Negative-staining EM and HS-AFM of chain particle (motor).** (A) Electron
606 micrograph of negatively stained chain particles. (B) Images of individual particles.
607 (C) Representative 2D averaged image. A mirror image is shown to match the
608 orientation of the hexameric ring observed by HS-AFM. (D) Illustration based on the
609 averaged image in panel C. Filamentous structures are marked by asterisks at an

610 end. The double-headed arrow shows the distance between the centers of the
611 hexamers. (E) Two patterns of HS-AFM images. The motor (chain particle) was
612 scanned at 56 × 56 pixels in an area of 70 × 70 nm^2 with a scanning rate of 100 ms
613 per frame. Illustrations for patterns I and II (left side) were depicted based on 3D
614 chain model shown in Fig. 5. Observation directions are indicated by arrows.
615 Protrusions are marked by blue triangles. Images of patterns I and II are shown in
616 green and purple frames, respectively. (F) Averaged images for patterns I (green
617 frame) and II (purple frame). The motor was scanned at 50 × 50 pixels in an area of
618 40 × 40 nm^2 with a scanning rate of 100 ms per frame. The images were produced
619 by averaging three successive video frames. (G) HS-AFM slice image showing two
620 hexameric rings (upper) and averaged EM image (lower). Upper: The red broken
621 boxed area in panel F was sliced for the height 9.8–11.3 nm from the substrate
622 surface, processed for smoothing, and magnified. The angle alignments of two
623 hexamers are schematically shown in the left upper. Lower: The central part of
624 panel C was excised and aligned to compare with the upper panel. Subunits of the
625 hexamer are marked by red circles. (H) Surface profiles along the lines in pattern I
626 (green) and II (purple). The upper and lower images in panel F were each profiled at
627 the green and purple lines passing the globule centers. The dimples and the peaks
628 are marked by open and black triangles, respectively. (I) Shedding process of the
629 peaks of pattern II particle shown in panel E. The peaks are marked by red triangles.
630 (J) Surface profile showing the disappeared peaks. The images in panel I were
631 each profiled at the clear blue, brown, and gray lines passing the globule centers.

632 The peaks are marked by black triangles. The double-headed arrows show the
633 peak heights. (K) HS-AFM image of the motor with seven lateral protrusions. The
634 motor was scanned at 120 × 120 pixels in an area of 120 × 120 nm^2 with a scanning
635 rate of 500 ms per frame. Lateral protrusions are indicated by blue triangles. (L)
636 Fluctuations of the protrusions of the particle shown in panel K. The images were
637 sliced for the height 0–7.0 nm from the substrate surface. The moving directions are
638 indicated by arrows. In all HS-AFM images, the color bar on the right shows the
639 range of image heights.
640
641 **FIG 4. Isolation of F_1-like ATPase unit.** (A) BN-PAGE of motors (chain particles)
642 treated with 1.5% sodium cholate (left) and In-gel ATPase activity assay (right).
643 Motors, motors treated with 1.5% sodium cholate (SC treatment), and thyroglobulin
644 were subjected to 3 to 12% gradient BN-PAGE. The band of the motor is marked by
645 a black triangle. The band of the ATPase unit revealed by sodium cholate treatment
646 is indicated by an open triangle. The white lead phosphate bands indicate ATPase
647 activity. Molecular masses are shown on the left. (B) Gel filtration assay using a
648 Sephacryl S-400 HR column. The light blue lines show a Gaussian fit. (C) The F1–
649 F13 fractions in the gel filtration assay indicated by the green line in panel B were
650 subjected to SDS-12.5% PAGE and stained with CBB. Bands for motor components
651 are marked by black triangles. (D) Comparison of band patterns between F6 and
652 the motor on CBB-stained SDS-12.5% PAGE. The position of F6 in the elution
653 volume is marked by a green triangle in panel B. (E) Electron micrograph of

654 negatively stained ATPase in F6. (F) Images of individual particles. (G)
655 Representative 2D averaged images (upper) and depictions of their structures
656 (lower). Upper: Hook structures in the hexameric ring and the stalks are marked by
657 green and orange triangles, respectively. Lower: The hexameric part, hook
658 structures and the stalk are colored rose, green and orange, respectively.
659
660 **FIG 5. Motor chain structure.** (A) Protein profile of chain fraction. CBB-stained
661 SDS-12.5% PAGE image of the crude chain fraction. The bands of motor
662 components, MMOBs 1670, 4530, 1660, 1630, and 1620 are marked by black
663 triangles from upper to lower. (B) Electron micrograph of negatively stained chains.
664 The chain structures are marked by blue lines. (C) Magnified chain images. (D)
665 Representative 2D averaged images. (E) Three-dimensional reconstruction of chain
666 containing two F_1-like ATPase dimers. The 3D map is visualized at a density
667 threshold (contour level = 0.026). The central stalks are marked by open triangles.
668 (F) Superposition of the atomic model of *Bacillus* F_1-ATPase catalytic $(\alpha\beta)_3$ (PDB ID
669 6N2Y) (37) onto the 3D chain structure. The α and β subunits are colored salmon
670 and turquoise, respectively. The central stalk and protrusions from hexameric rings
671 are marked by open and black triangles, respectively. (G) Cross section of
672 mushroom-like structures. Central stalks are marked by broken circles. The
673 double-headed arrow shows the length of the protrusion. Corresponding
674 mushroom-like structures are marked (a)–(d) in panel F. (H) Comparison between
675 the motor image from Fig. 3C (left) and the chain reprojection (middle). The

reprojected image is viewed from the angle used for the right image of panel E. Short filaments corresponding to the position of the connecting bulge are marked by asterisks. A depiction of the chain model based on the comparison (right). (I) Comparison between the averaged chain image from ECT (left) and the chain reprojection (middle). Left image was modified from (23). The chain was reprojected from an angle close to the middle image in panel E. Inner sides and membrane relative to the chain are marked by i and m, respectively. The protrusion from the globule corresponding to the central stalk from the hexameric ring, one from the connecting bulge and the globule attached to the connecting bulge are marked by orange, light blue and green triangles, respectively. The areas of image densities that were visualized only in the ECT image are marked by broken lines. An illustration depicts a chain model based on the comparison (right).

FIG 6. Working models for force transmission mechanism. The gliding direction is indicated by a red arrow. The regions marked in gray were visualized only in the ECT image. The crank protein Gli521 and the leg protein Gli349 are colored green and red, respectively. (i) Contraction model: The force generated by the hexameric ring displaces the motor along the gliding direction. The displacements are transmitted through the membrane to Gli521. (ii) Rotation model: The force generated by the hexameric ring rotates the central stalk in a mechanism similar to that of F_1-ATPase. The rotational motion is transmitted across the membrane to Gli521.The generation and transmission of forces are presented by black arrows for

both models.

FIG S1 Conditions to solubilize chain particle. The Triton-insoluble fraction was treated with buffers containing the specified concentrations of NaCl and centrifuged. The Triton-insoluble fraction (TI), the supernatants (S) and the pellets (P) were analyzed by SDS-12.5% PAGE. MMOB1670, a component of the chain, is marked by a black triangle. Molecular masses are shown on the left.

FIG S2 Two-dimensional averaged images of chain particle obtained by negative-staining EM. Four classes of clear particle images from 20 classes are represented. As mentioned in Fig. 3C, they were mirrored.

FIG S3 Protein profiles of gel-filtration fractions visualized by reverse-staining method. Motor components are marked by black triangles on the right. Molecular masses are shown on the left. Fractions F10–F13 correspond to the first half of the large three peaks in the elution volume from 80–100 mL shown in Fig. 4B.

FIG S4 Two-dimensional averaged images of globular complex in F6. Fifteen classes of clear particle images from 50 classes are represented.

FIG S5 Reprojection images of chain. Two-dimensional averaged images (upper) and the corresponding reprojection images (lower) calculated from the 3D map of

the chain are compared.

Movie S1 HS-AFM movie showing pattern I particles The particles were scanned at 10 fps. The scanning field was 70 × 70 nm^2 with 56 × 56 pixels. The video was played at 10 fps.

Movie S2 HS-AFM movie showing pattern II particles The particles were scanned at 10 fps. The scanning field was 70 × 70 nm^2 with 56 × 56 pixels. The video was played at 10 fps.

Movie S3 HS-AFM movie showing the shedding process of the peaks. The particles were scanned at 10 fps. The scanning field was 70 × 70 nm^2 with 56 × 56 pixels. The video was played at 10 fps. The peaks are indicated by the red triangles.

Movie S4 HS-AFM movie showing fluctuations in protrusions. The particles were scanned at 2 fps. The scanning field was 120 × 120 nm^2 with 120 × 120 pixels. The video was played at 1 fps. The protrusions are indicated by the red triangles.

References

1. Razin S, Hayflick L. 2010. Highlights of mycoplasma research--an historical perspective. Biologicals 38:183-90.
2. Grosjean H, Breton M, Sirand-Pugnet P, Tardy F, Thiaucourt F, Citti C, Barre A, Yoshizawa S, Fourmy D, de Crecy-Lagard V, Blanchard A. 2014.

Predicting the minimal translation apparatus: lessons from the reductive evolution of mollicutes. PLoS Genet 10:e1004363.

3. Miyata M, Robinson RC, Uyeda TQP, Fukumori Y, Fukushima SI, Haruta S, Homma M, Inaba K, Ito M, Kaito C, Kato K, Kenri T, Kinosita Y, Kojima S, Minamino T, Mori H, Nakamura S, Nakane D, Nakayama K, Nishiyama M, Shibata S, Shimabukuro K, Tamakoshi M, Taoka A, Tashiro Y, Tulum I, Wada H, Wakabayashi KI. 2020. Tree of motility - A proposed history of motility systems in the tree of life. Genes Cells 25:6-21.
4. Miyata M. 2010. Unique centipede mechanism of *Mycoplasma* gliding. Annu Rev Microbiol 64:519-37.
5. Miyata M, Hamaguchi T. 2016. Prospects for the gliding mechanism of *Mycoplasma mobile*. Curr Opin Microbiol 29:15-21.
6. Miyata M, Hamaguchi T. 2016. Integrated information and prospects for gliding mechanism of the pathogenic bacterium *Mycoplasma pneumoniae*. Front Microbiol 7:960.
7. Uenoyama A, Kusumoto A, Miyata M. 2004. Identification of a 349-kilodalton protein (Gli349) responsible for cytadherence and glass binding during gliding of *Mycoplasma mobile*. J Bacteriol 186:1537-45.
8. Seto S, Uenoyama A, Miyata M. 2005. Identification of a 521-kilodalton protein (Gli521) involved in force generation or force transmission for *Mycoplasma mobile* gliding. J Bacteriol 187:3502-10.
9. Uenoyama A, Miyata M. 2005. Identification of a 123-kilodalton protein (Gli123) involved in machinery for gliding motility of *Mycoplasma mobile*. J Bacteriol 187:5578-84.
10. Uenoyama A, Seto S, Nakane D, Miyata M. 2009. Regions on Gli349 and Gli521 protein molecules directly involved in movements of *Mycoplasma mobile* gliding machinery, suggested by use of inhibitory antibodies and mutants. J Bacteriol 191:1982-5.
11. Kusumoto A, Seto S, Jaffe JD, Miyata M. 2004. Cell surface differentiation of *Mycoplasma mobile* visualized by surface protein localization. Microbiology 150:4001-8.
12. Miyata M, Petersen JD. 2004. Spike structure at the interface between gliding *Mycoplasma mobile* cells and glass surfaces visualized by

776 rapid-freeze-and-fracture electron microscopy. J Bacteriol 186:4382-6.
777 13. Adan-Kubo J, Uenoyama A, Arata T, Miyata M. 2006. Morphology of isolated
778 Gli349, a leg protein responsible for *Mycoplasma mobile* gliding via glass
779 binding, revealed by rotary shadowing electron microscopy. J Bacteriol
780 188:2821-8.
781 14. Lesoil C, Nonaka T, Sekiguchi H, Osada T, Miyata M, Afrin R, Ikai A. 2010.
782 Molecular shape and binding force of *Mycoplasma mobile*'s leg protein
783 Gli349 revealed by an AFM study. Biochem Biophys Res Commun
784 391:1312-7.
785 15. Metsugi S, Uenoyama A, Adan-Kubo J, Miyata M, Yura K, Kono H, Go N.
786 2005. Sequence analysis of the gliding protein Gli349 in *Mycoplasma mobile*.
787 Biophysics (Nagoya-shi) 1:33-43.
788 16. Hamaguchi T, Kawakami M, Furukawa H, Miyata M. 2019. Identification of
789 novel protein domain for sialyloligosaccharide binding essential to
790 *Mycoplasma mobile* gliding. FEMS Microbiol Lett 366:fnz016.
791 17. Morio H, Kasai T, Miyata M. 2016. Gliding direction of *Mycoplasma mobile*. J
792 Bacteriol 198:283-90.
793 18. Kasai T, Hamaguchi T, Miyata M. 2015. Gliding motility of *Mycoplasma*
794 *mobile* on uniform oligosaccharides. J Bacteriol 197:2952-7.
795 19. Kasai T, Nakane D, Ishida H, Ando H, Kiso M, Miyata M. 2013. Role of
796 binding in *Mycoplasma mobile* and *Mycoplasma pneumoniae* gliding
797 analyzed through inhibition by synthesized sialylated compounds. J Bacteriol
798 195:429-35.
799 20. Nagai R, Miyata M. 2006. Gliding motility of *Mycoplasma mobile* can occur by
800 repeated binding to *N*-acetylneuraminyllactose (sialyllactose) fixed on solid
801 surfaces. J Bacteriol 188:6469-75.
802 21. Chen J, Neu J, Miyata M, Oster G. 2009. Motor-substrate interactions in
803 *Mycoplasma* motility explains non-Arrhenius temperature dependence.
804 Biophys J 97:2930-8.
805 22. Mizutani M, Tulum I, Kinosita Y, Nishizaka T, Miyata M. 2018. Detailed
806 analyses of stall force generation in *Mycoplasma mobile* gliding. Biophys J
807 114:1411-1419.
808 23. Nishikawa M, Nakane D, Toyonaga T, Kawamoto A, Kato T, Namba K, Miyata

M. 2019. Refined mechanism of *Mycoplasma mobile* gliding based on structure, ATPase activity, and sialic acid binding of machinery. mBio 10:e02846-19.

24. Nakane D, Miyata M. 2007. Cytoskeletal "jellyfish" structure of *Mycoplasma mobile*. Proc Natl Acad Sci U S A 104:19518-23.

25. Tulum I, Yabe M, Uenoyama A, Miyata M. 2014. Localization of P42 and F_1-ATPase alpha-subunit homolog of the gliding machinery in *Mycoplasma mobile* revealed by newly developed gene manipulation and fluorescent protein tagging. J Bacteriol 196:1815-24.

26. Tulum I, Kimura K, Miyata M. 2020. Identification and sequence analyses of the gliding machinery proteins from *Mycoplasma mobile*. Sci Rep 10:3792.

27. Walker JE, Saraste M, Runswick MJ, Gay NJ. 1982. Distantly related sequences in the alpha- and beta-subunits of ATP synthase, myosin, kinases and other ATP-requiring enzymes and a common nucleotide binding fold. Embo j 1:945-51.

28. Abrahams JP, Leslie AG, Lutter R, Walker JE. 1994. Structure at 2.8 A resolution of F1-ATPase from bovine heart mitochondria. Nature 370:621-8.

29. Kühlbrandt W. 2019. Structure and Mechanisms of F-Type ATP Synthases. Annu Rev Biochem 88:515-549.

30. Beven L, Charenton C, Dautant A, Bouyssou G, Labroussaa F, Skollermo A, Persson A, Blanchard A, Sirand-Pugnet P. 2012. Specific evolution of F_1-like ATPases in mycoplasmas. PLoS One 7:e38793.

31. Nottelet P, Bataille L, Gourgues G, Anger R, Lartigue C, Sirand-Pugnet P, Marza E, Fronzes R, Arfi Y. 2021. The mycoplasma surface proteins MIB and MIP promote the dissociation of the antibody-antigen interaction. Sci Adv 7.

32. Kobayashi K, Kodera N, Kasai T, Tahara YO, Toyonaga T, Mizutani M, Fujiwara I, Ando T, Miyata M. 2021. Movements of *Mycoplasma mobile* gliding machinery detected by high-speed atomic force microscopy. bioRxiv doi:10.1101/2021.01.28.428740:2021.01.28.428740.

33. Bowler MW, Montgomery MG, Leslie AG, Walker JE. 2006. How azide inhibits ATP hydrolysis by the F-ATPases. Proc Natl Acad Sci U S A 103:8646-9.

34. Zivanov J, Nakane T, Forsberg BO, Kimanius D, Hagen WJ, Lindahl E,

Scheres SH. 2018. New tools for automated high-resolution cryo-EM structure determination in RELION-3. eLife 7:e42166.

35. Ando T. 2018. High-speed atomic force microscopy and its future prospects. Biophys Rev 10:285-292.

36. Uchihashi T, Iino R, Ando T, Noji H. 2011. High-speed atomic force microscopy reveals rotary catalysis of rotorless F_1-ATPase. Science 333:755-8.

37. Guo H, Suzuki T, Rubinstein JL. 2019. Structure of a bacterial ATP synthase. eLife 8:e43128.

38. Cheng Y, Wolf E, Larvie M, Zak O, Aisen P, Grigorieff N, Harrison SC, Walz T. 2006. Single particle reconstructions of the transferrin-transferrin receptor complex obtained with different specimen preparation techniques. J Mol Biol 355:1048-65.

39. Dibrova DV, Konovalov KA, Perekhvatov VV, Skulachev KV, Mulkidjanian AY. 2017. COGcollator: a web server for analysis of distant relationships between homologous protein families. Biol Direct 12:29.

40. Neuwald AF, Aravind L, Spouge JL, Koonin EV. 1999. AAA+: A class of chaperone-like ATPases associated with the assembly, operation, and disassembly of protein complexes. Genome Res 9:27-43.

41. Snider J, Thibault G, Houry WA. 2008. The AAA+ superfamily of functionally diverse proteins. Genome Biol 9:216.

42. Minauro-Sanmiguel F, Wilkens S, García JJ. 2005. Structure of dimeric mitochondrial ATP synthase: novel F0 bridging features and the structural basis of mitochondrial cristae biogenesis. Proc Natl Acad Sci U S A 102:12356-8.

43. Allegretti M, Klusch N, Mills DJ, Vonck J, Kühlbrandt W, Davies KM. 2015. Horizontal membrane-intrinsic α-helices in the stator a-subunit of an F-type ATP synthase. Nature 521:237-40.

44. Blum TB, Hahn A, Meier T, Davies KM, Kühlbrandt W. 2019. Dimers of mitochondrial ATP synthase induce membrane curvature and self-assemble into rows. Proc Natl Acad Sci U S A 116:4250-4255.

45. Tanaka A, Nakane D, Mizutani M, Nishizaka T, Miyata M. 2016. Directed binding of gliding bacterium, *Mycoplasma mobile*, shown by detachment

force and bond lifetime. mBio 7:00455-16.

46. Noji H, Ueno H, McMillan DGG. 2017. Catalytic robustness and torque generation of the F_1-ATPase. Biophys Rev 9:103-118.

47. Naito TM, Masaike T, Nakane D, Sugawa M, Okada KA, Nishizaka T. 2019. Single-molecule pull-out manipulation of the shaft of the rotary motor F_1-ATPase. Sci Rep 9:7451.

48. Watson HC, Walker NP, Shaw PJ, Bryant TN, Wendell PL, Fothergill LA, Perkins RE, Conroy SC, Dobson MJ, Tuite MF. 1982. Sequence and structure of yeast phosphoglycerate kinase. Embo j 1:1635-40.

49. Jaffe JD, Stange-Thomann N, Smith C, DeCaprio D, Fisher S, Butler J, Calvo S, Elkins T, FitzGerald MG, Hafez N, Kodira CD, Major J, Wang S, Wilkinson J, Nicol R, Nusbaum C, Birren B, Berg HC, Church GM. 2004. The complete genome and proteome of *Mycoplasma mobile*. Genome Res 14:1447-61.

50. Lu M, Holliday LS, Zhang L, Dunn WA, Jr., Gluck SL. 2001. Interaction between aldolase and vacuolar H^+-ATPase: evidence for direct coupling of glycolysis to the ATP-hydrolyzing proton pump. J Biol Chem 276:30407-13.

51. Lu M, Ammar D, Ives H, Albrecht F, Gluck SL. 2007. Physical interaction between aldolase and vacuolar H^+-ATPase is essential for the assembly and activity of the proton pump. J Biol Chem 282:24495-503.

52. Chan CY, Dominguez D, Parra KJ. 2016. Regulation of Vacuolar H^+-ATPase (V-ATPase) Reassembly by Glycolysis Flow in 6-Phosphofructo-1-kinase (PFK-1)-deficient Yeast Cells. J Biol Chem 291:15820-9.

53. Kinosita Y, Nakane D, Sugawa M, Masaike T, Mizutani K, Miyata M, Nishizaka T. 2014. Unitary step of gliding machinery in Mycoplasma mobile. Proc Natl Acad Sci U S A 111:8601-6.

54. Kinosita Y, Miyata M, Nishizaka T. 2018. Linear motor driven-rotary motion of a membrane-permeabilized ghost in *Mycoplasma mobile*. Sci Rep 8:11513.

55. Uenoyama A, Miyata M. 2005. Gliding ghosts of *Mycoplasma mobile*. Proc Natl Acad Sci USA 102:12754-8.

56. Miyata M, Yamamoto H, Shimizu T, Uenoyama A, Citti C, Rosengarten R. 2000. Gliding mutants of *Mycoplasma mobile*: relationships between motility and cell morphology, cell adhesion and microcolony formation. Microbiology 146:1311-20.

908 57. Aluotto BB, Wittler RG, Williams CO, Faber JE. 1970. Standardized
909 bacteriologic techniques for the characterization of *Mycoplasma* species. Int
910 J Syst Bacteriol 20:35-58.
911 58. Kawakita Y, Kinoshita M, Furukawa Y, Tulum I, Tahara YO, Katayama E,
912 Namba K, Miyata M. 2016. Structural study of MPN387, an essential protein
913 for gliding motility of a human-pathogenic bacterium, *Mycoplasma*
914 *pneumoniae*. J Bacteriol 198:2352-9.
915 59. Lee C, Levin A, Branton D. 1987. Copper staining: a five-minute protein stain
916 for sodium dodecyl sulfate-polyacrylamide gels. Anal Biochem 166:308-12.
917 60. Dzandu JK, Johnson JF, Wise GE. 1988. Sodium dodecyl sulfate-gel
918 electrophoresis: staining of polypeptides using heavy metal salts. Anal
919 Biochem 174:157-67.
920 61. Zerbetto E, Vergani L, Dabbeni-Sala F. 1997. Quantification of muscle
921 mitochondrial oxidative phosphorylation enzymes via histochemical staining
922 of blue native polyacrylamide gels. Electrophoresis 18:2059-64.
923 62. Wittig I, Schägger H. 2005. Advantages and limitations of clear-native PAGE.
924 Proteomics 5:4338-46.
925 63. Webb MR. 1992. A continuous spectrophotometric assay for inorganic
926 phosphate and for measuring phosphate release kinetics in biological
927 systems. Proc Natl Acad Sci U S A 89:4884-7.
928 64. Zhang K. 2016. Gctf: Real-time CTF determination and correction. J Struct
929 Biol 193:1-12.
930 65. Pettersen EF, Goddard TD, Huang CC, Couch GS, Greenblatt DM, Meng EC,
931 Ferrin TE. 2004. UCSF Chimera--a visualization system for exploratory
932 research and analysis. J Comput Chem 25:1605-12.
933 66. Ando T, Kodera N, Takai E, Maruyama D, Saito K, Toda A. 2001. A
934 high-speed atomic force microscope for studying biological macromolecules.
935 Proc Natl Acad Sci U S A 98:12468-72.
936 67. Uchihashi T, Kodera N, Ando T. 2012. Guide to video recording of structure
937 dynamics and dynamic processes of proteins by high-speed atomic force
938 microscopy. Nat Protoc 7:1193-206.
939 68. Ngo KX, Kodera N, Katayama E, Ando T, Uyeda TQ. 2015. Cofilin-induced
940 unidirectional cooperative conformational changes in actin filaments revealed

941 by high-speed atomic force microscopy. eLife 4:e04806.
942

Figure 1

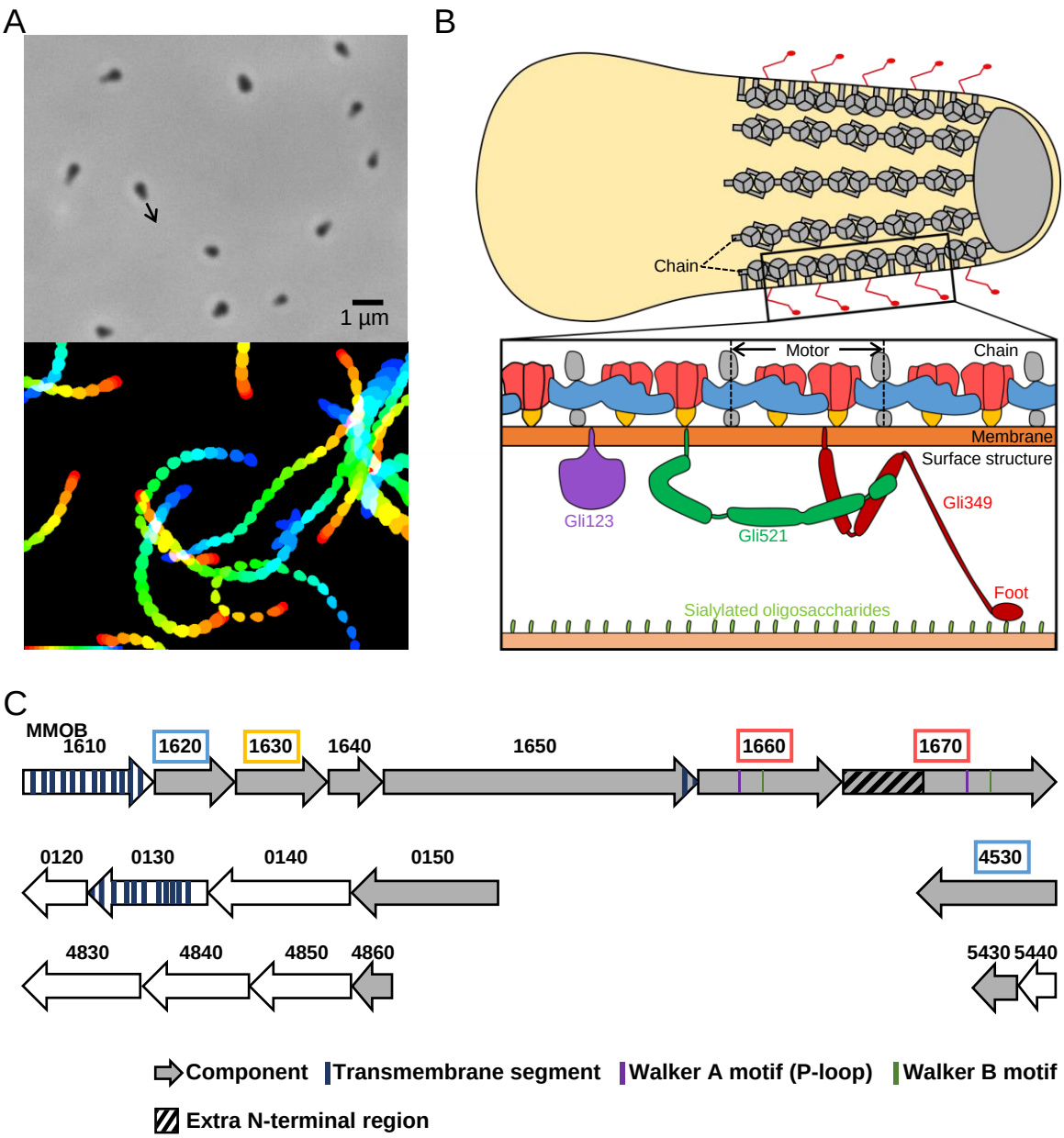

FIG 1. Gliding machinery of *Mycoplasma mobile*. (A) Optical microscopy of cells (upper) and trajectories of gliding cells (lower). The gliding direction is indicated by a black arrow. The 4-second trajectory is colored from red to blue. (B) Schematic illustration of gliding machinery based on the present study. In the whole cell shown in upper illustration, the internal structure and legs are colored gray and red, respectively. The actual cell has about 28 chains, each consisting of 17 particles, although a more limited number is illustrated here. A single unit of the surface structure and a chain of the internal structure are magnified in the lower illustration. “Motor” is identical to “chain particle.” (C) ORFs for the internal structure. The components of the internal structure are colored gray. Type 2 ATPase operon is at the top. Motor components revealed in the present study are marked by colored boxes, corresponding to the colored components of the lower illustration in panel B.

Figure 2

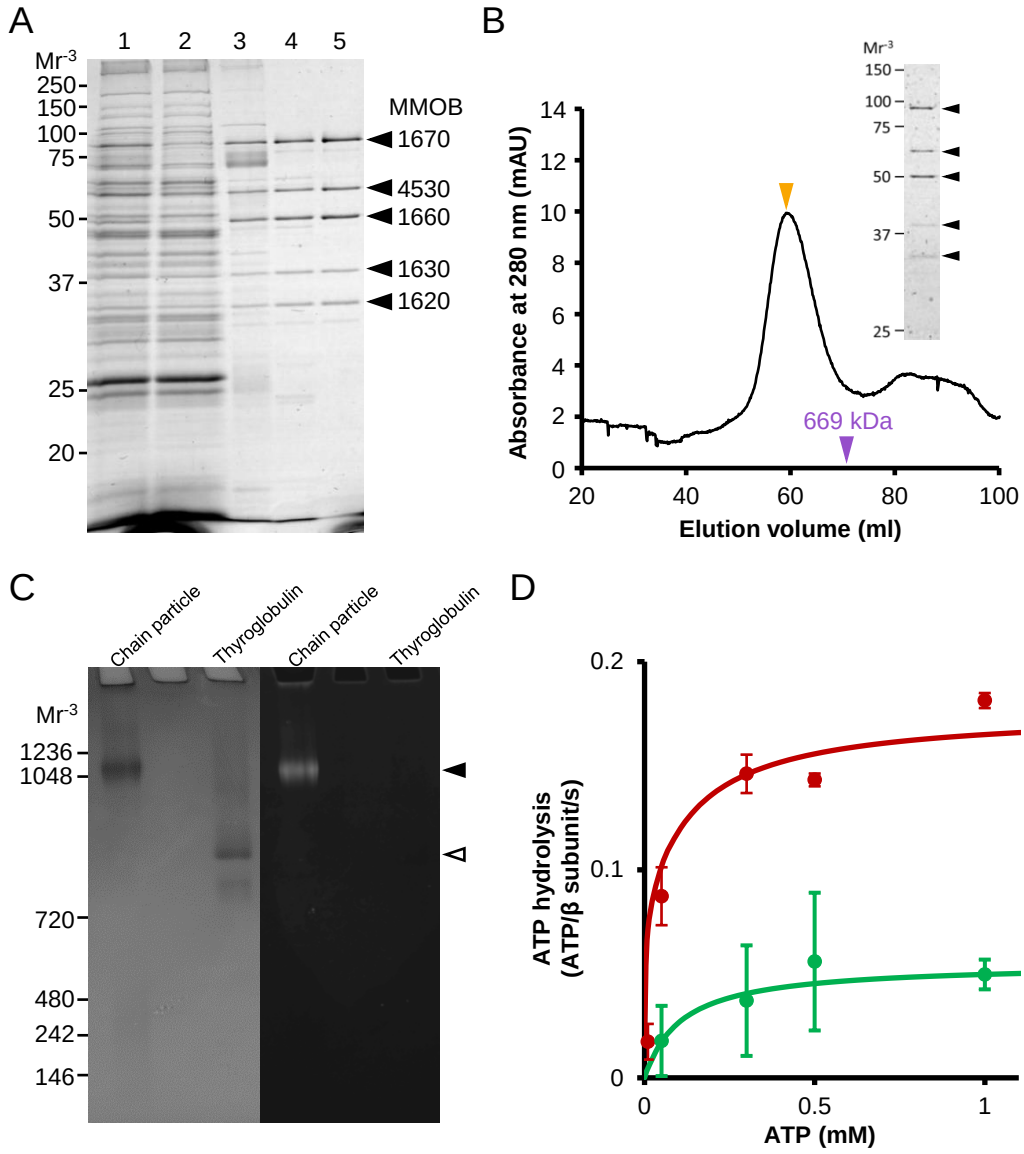

FIG 2. Isolation profile and characterization of chain particle. (A) Protein profile of each fraction. The fractions were subjected to SDS-12.5% PAGE gel and stained with CBB. Lane 1, lysate of *M. mobile* cells; lane 2, Triton-soluble fraction; lane 3, Triton-insoluble fraction; lane 4, supernatant after incubation in a buffer containing 137 mM NaCl; lane 5, peak fraction of Superdex 200 gel filtration chromatography. The bands of the chain particle components are marked by black triangles. Molecular masses are shown on the left. (B) Gel filtration assay using Sephacryl S-400 HR column. The peak position of thyroglobulin (669 kDa) is marked by a purple triangle. The peak fraction of the chain particles marked by an orange triangle was analyzed by SDS-12.5% PAGE. The bands of the chain particle components are marked by black triangles. (C) BN-PAGE (left) and In-gel ATPase activity assay (right). Isolated chain particle and thyroglobulin, which has no ATPase activity, were subjected to 3 to 12% gradient BN-PAGE. The band positions of the chain particle and thyroglobulin are marked by black and open triangles, respectively. White precipitates, indicating ATPase activity, appeared only at the band position of the chain particle. Molecular masses are shown on the left. (D) Phosphate release assay under various ATP concentrations with and without sodium azide. The ATPase activities under 0- and 15.4-mM sodium azide are marked by red and green filled circles, respectively (n = 3). These data were fitted by the Michaelis-Menten equation as solid lines.

Figure 3

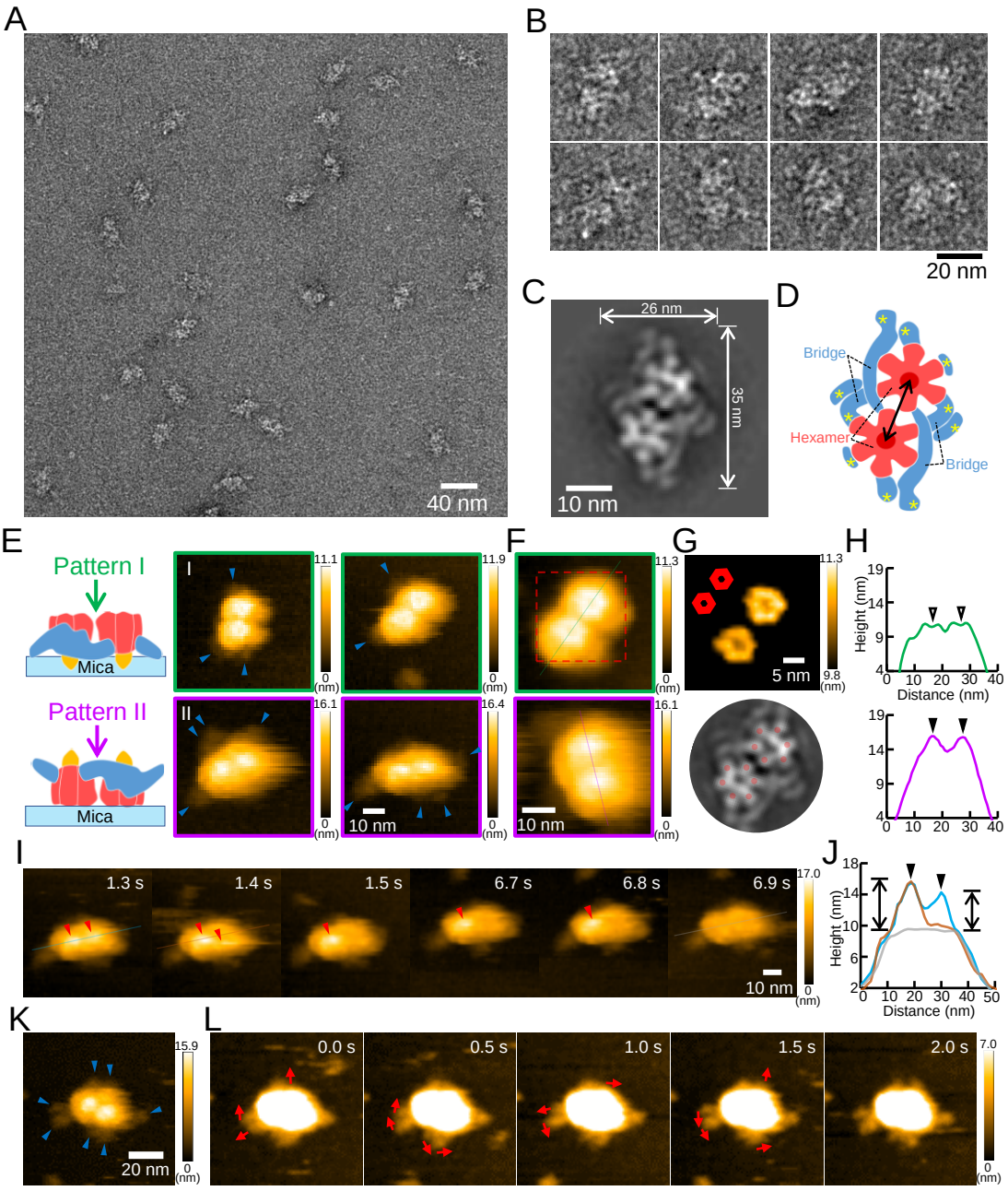

FIG 3. Negative-staining EM and HS-AFM of chain particle (motor). (A) Electron micrograph of negatively stained chain particles. (B) Images of individual particles. (C) Representative 2D averaged image. A mirror image is shown to match the orientation of the hexameric ring observed by HS-AFM. (D) Illustration based on the averaged image in panel C. Filamentous structures are marked by asterisks at an end. The double-headed arrow shows the distance between the centers of the hexamers. (E) Two patterns of HS-AFM images. The motor (chain particle) was scanned at 56 × 56 pixels in an area of 70 × 70 nm^2 with a scanning rate of 100 ms per frame. Illustrations for patterns I and II (left side) were depicted based on 3D chain model shown in Fig. 5. Observation directions are indicated by arrows. Protrusions are marked by blue triangles. Images of patterns I and II are shown in green and purple frames, respectively. (F) Averaged images for patterns I (green frame) and II (purple frame). The motor was scanned at 50 × 50 pixels in an area of 40 × 40 nm^2 with a scanning rate of 100 ms per frame. The images were produced by averaging three successive video frames. (G) HS-AFM slice image showing two hexameric rings (upper) and averaged EM image (lower). Upper: The red broken boxed area in panel F was sliced for the height 9.8–11.3 nm from the substrate surface, processed for smoothing, and magnified. The angle alignments of two hexamers are schematically shown in the left upper. Lower: The central part of panel C was excised and aligned to compare with the upper panel. Subunits of the hexamer are marked by red circles. (H) Surface profiles along the lines in pattern I (green) and II (purple). The upper and lower images in panel F were each profiled at the green and purple lines passing the globule centers. The dimples and the peaks are marked by open and black triangles, respectively. (I) Shedding process of the peaks of pattern II particle shown in panel E. The peaks are marked by red triangles. (J) Surface profile showing the disappeared peaks. The images in panel I were each profiled at the clear blue, brown, and gray lines passing the globule centers. The peaks are marked by black triangles. The double-headed arrows show the peak heights. (K) HS-AFM image of the motor with seven lateral protrusions. The motor was scanned at 120 × 120 pixels in an area of 120 × 120 nm^2 with a scanning rate of 500 ms per frame. Lateral protrusions are indicated by blue triangles. (L) Fluctuations of the protrusions of the particle shown in panel K. The images were sliced for the height 0–7.0 nm from the substrate surface. The moving directions are indicated by arrows. In all HS-AFM images, the color bar on the right shows the range of image heights.

Figure 4

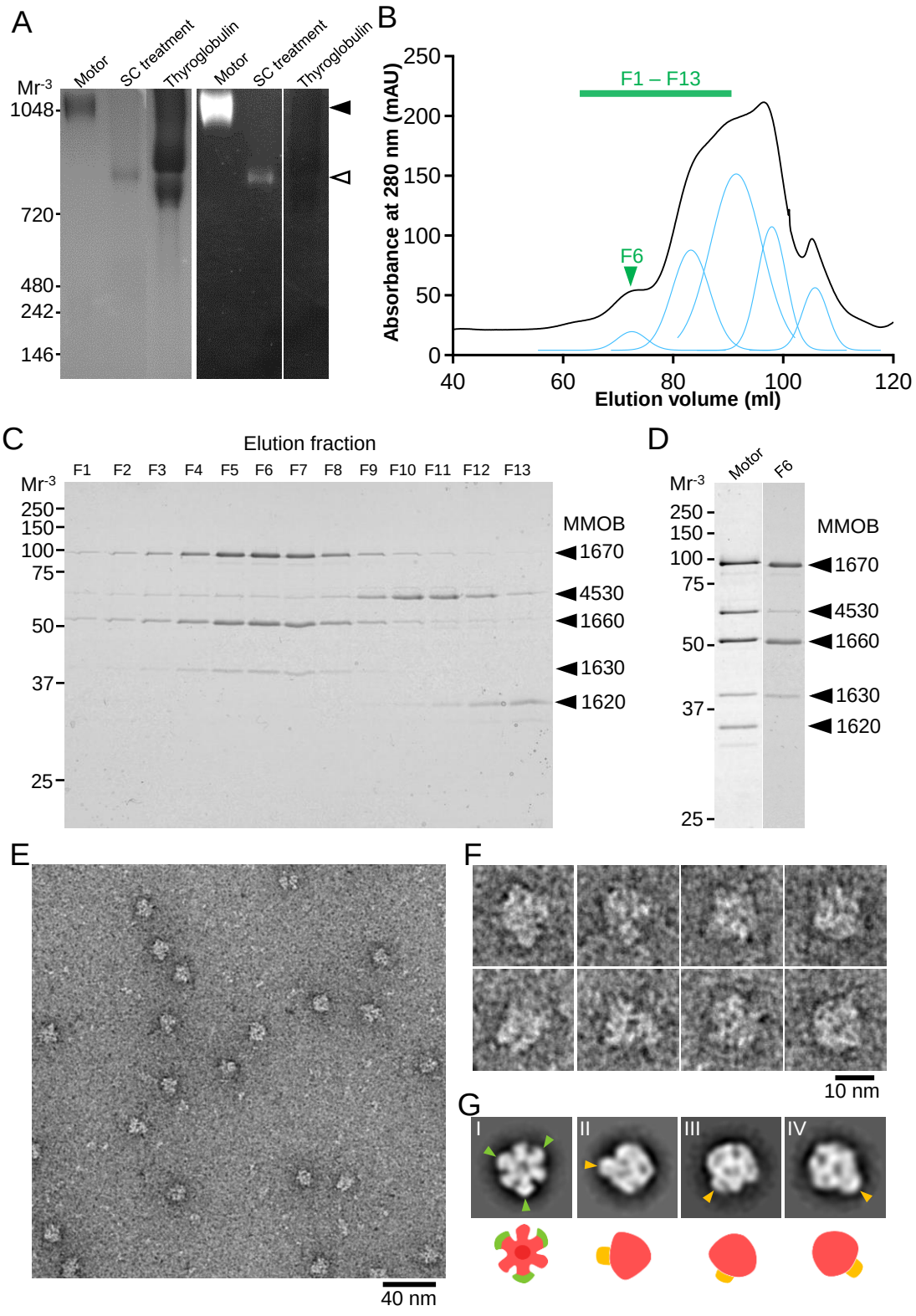

FIG 4. Isolation of F_1-like ATPase unit. (A) BN-PAGE of motors (chain particles) treated with 1.5% sodium cholate (left) and In-gel ATPase activity assay (right). Motors, motors treated with 1.5% sodium cholate (SC treatment), and thyroglobulin were subjected to 3 to 12% gradient BN-PAGE. The band of the motor is marked by a black triangle. The band of the ATPase unit revealed by sodium cholate treatment is indicated by an open triangle. The white lead phosphate bands indicate ATPase activity. Molecular masses are shown on the left. (B) Gel filtration assay using a Sephacryl S-400 HR column. The light blue lines show a Gaussian fit. (C) The F1–F13 fractions in the gel filtration assay indicated by the green line in panel B were subjected to SDS-12.5% PAGE and stained with CBB. Bands for motor components are marked by black triangles. (D) Comparison of band patterns between F6 and the motor on CBB-stained SDS-12.5% PAGE. The position of F6 in the elution volume is marked by a green triangle in panel B. (E) Electron micrograph of negatively stained ATPase in F6. (F) Images of individual particles. (G) Representative 2D averaged images (upper) and depictions of their structures (lower). Upper: Hook structures in the hexameric ring and the stalks are marked by green and orange triangles, respectively. Lower: The hexameric part, hook structures and the stalk are colored rose, green and orange, respectively.

Figure 5

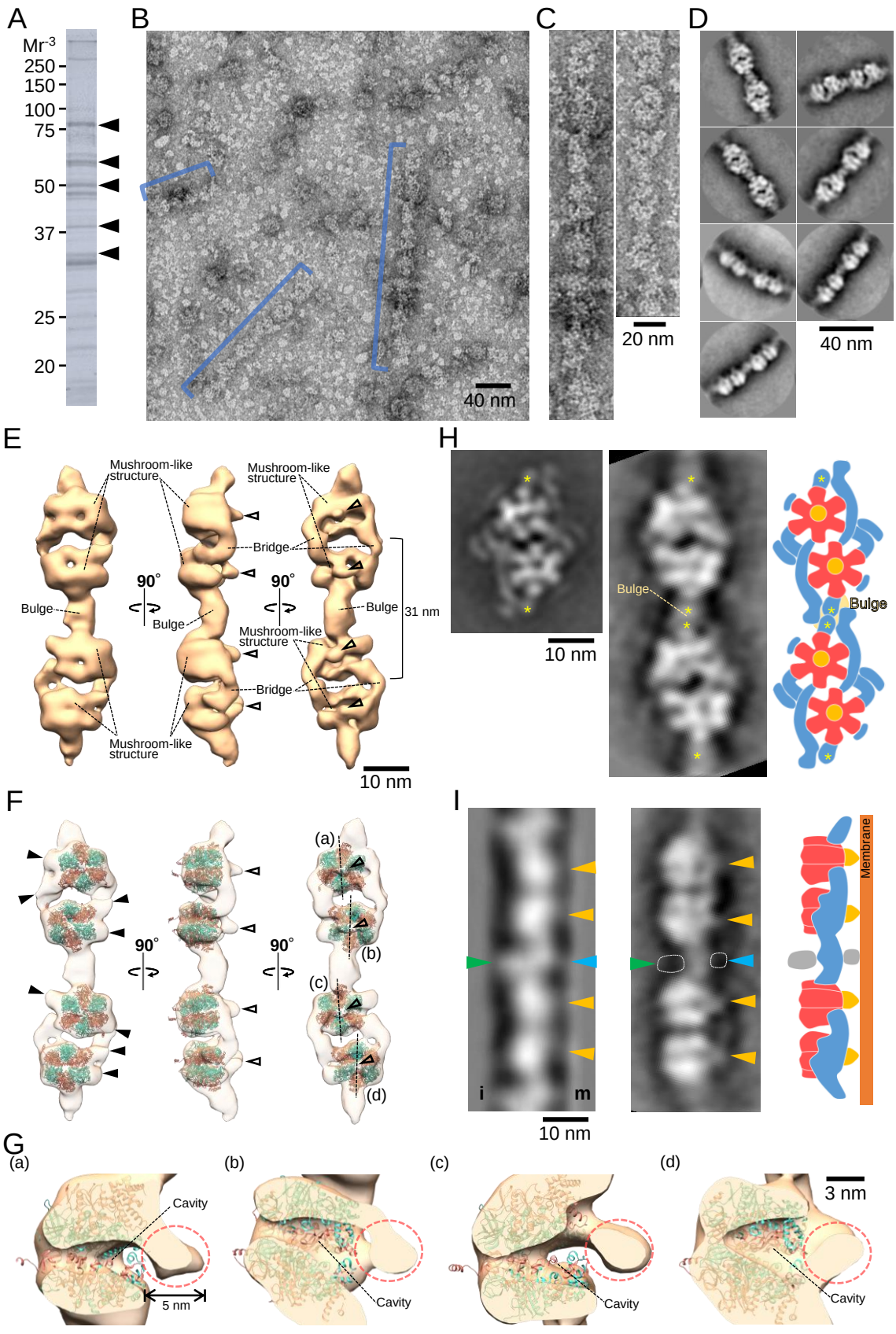

FIG 5. Motor chain structure. (A) Protein profile of chain fraction. CBB-stained SDS-12.5% PAGE image of the crude chain fraction. The bands of motor components, MMOBs 1670, 4530, 1660, 1630, and 1620 are marked by black triangles from upper to lower. (B) Electron micrograph of negatively stained chains. The chain structures are marked by blue lines. (C) Magnified chain images. (D) Representative 2D averaged images. (E) Three-dimensional reconstruction of chain containing two F_1-like ATPase dimers. The 3D map is visualized at a density threshold (contour level = 0.026). The central stalks are marked by open triangles. (F) Superposition of the atomic model of *Bacillus* F_1-ATPase catalytic $(\alpha\beta)_3$ (PDB ID 6N2Y) (37) onto the 3D chain structure. The α and β subunits are colored salmon and turquoise, respectively. The central stalk and protrusions from hexameric rings are marked by open and black triangles, respectively. (G) Cross section of mushroom-like structures. Central stalks are marked by broken circles. The double-headed arrow shows the length of the protrusion. Corresponding mushroom-like structures are marked (a)–(d) in panel F. (H) Comparison between the motor image from Fig. 3C (left) and the chain reprojection (middle). The reprojected image is viewed from the angle used for the right image of panel E. Short filaments corresponding to the position of the connecting bulge are marked by asterisks. A depiction of the chain model based on the comparison (right). (I) Comparison between the averaged chain image from ECT (left) and the chain reprojection (middle). Left image was modified from (23). The chain was reprojected from an angle close to the middle image in panel E. Inner sides and membrane relative to the chain are marked by i and m, respectively. The protrusion from the globule corresponding to the central stalk from the hexameric ring, one from the connecting bulge and the globule attached to the connecting bulge are marked by orange, light blue and green triangles, respectively. The areas of image densities that were visualized only in the ECT image are marked by broken lines. An illustration depicts a chain model based on the comparison (right).

Figure 6

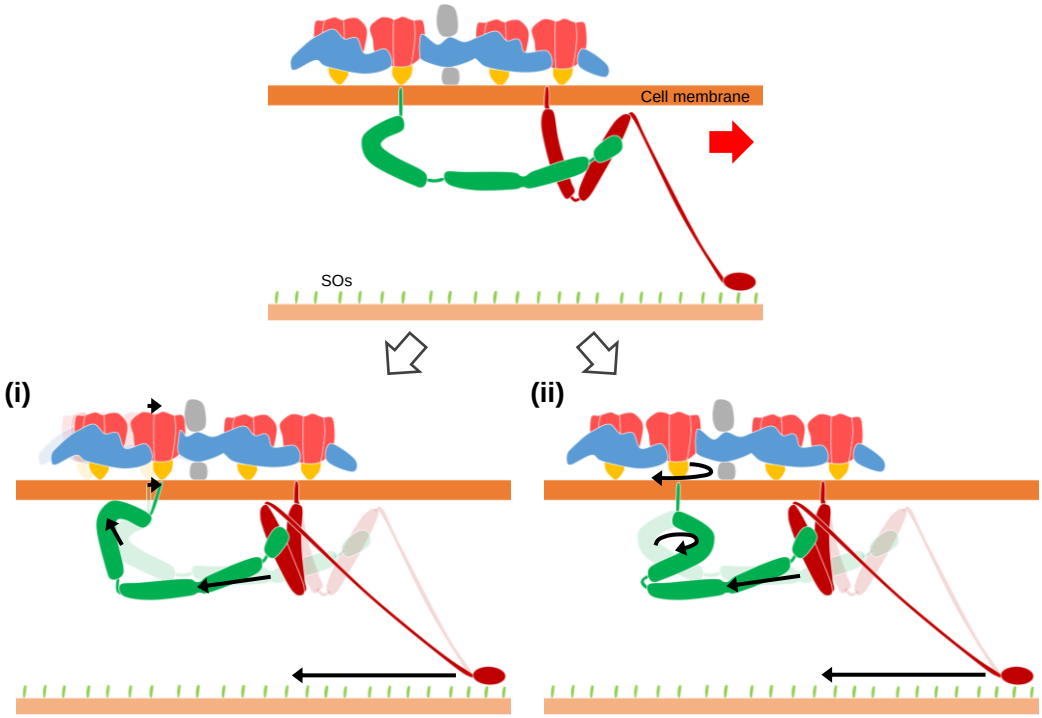

FIG 6. Working models for force transmission mechanism. The gliding direction is indicated by a red arrow. The regions marked in gray were visualized only in the ECT image. The crank protein Gli521 and the leg protein Gli349 are colored green and red, respectively. (i) Contraction model: The force generated by the hexameric ring displaces the motor along the gliding direction. The displacements are transmitted through the membrane to Gli521. (ii) Rotation model: The force generated by the hexameric ring rotates the central stalk in a mechanism similar to that of F_1-ATPase. The rotational motion is transmitted across the membrane to Gli521.The generation and transmission of forces are presented by black arrows for both models.

Supplementary figure 1

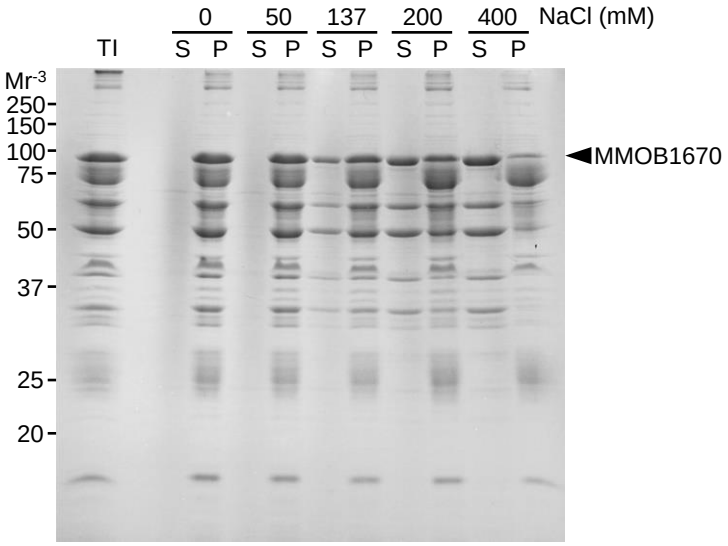

FIG S1 Conditions to solubilize chain particle. The Triton-insoluble fraction was treated with buffers containing the specified concentrations of NaCl and centrifuged. The Triton-insoluble fraction (TI), the supernatants (S) and the pellets (P) were analyzed by SDS-12.5% PAGE. MMOB1670, a component of the chain, is marked by a black triangle. Molecular masses are shown on the left.

Supplementary figure 2

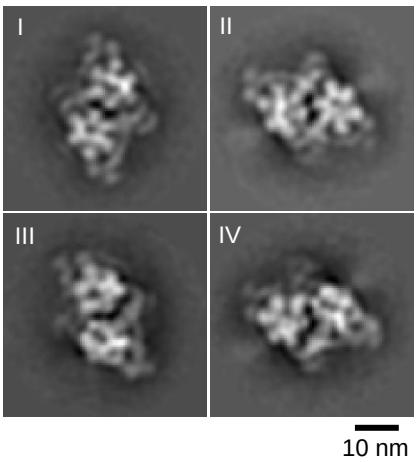

FIG S2 Two-dimensional averaged images of chain particle obtained by negative-staining EM. Four classes of clear particle images from 20 classes are represented. As mentioned in Fig. 3C, they were mirrored.

Supplementary figure 3

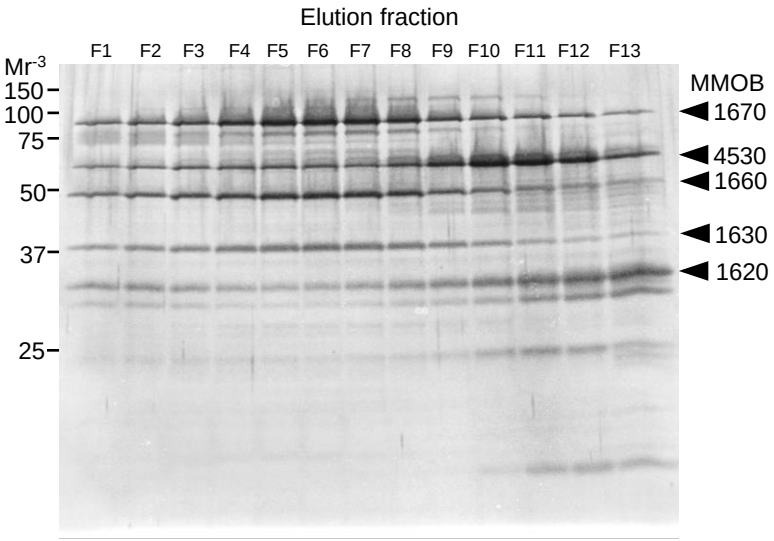

FIG S3 Protein profiles of gel-filtration fractions visualized by reverse-staining method. Motor components are marked by black triangles on the right. Molecular masses are shown on the left. Fractions F10–F13 correspond to the first half of the large three peaks in the elution volume from 80–100 mL shown in Fig. 4B.

Supplementary figure 4

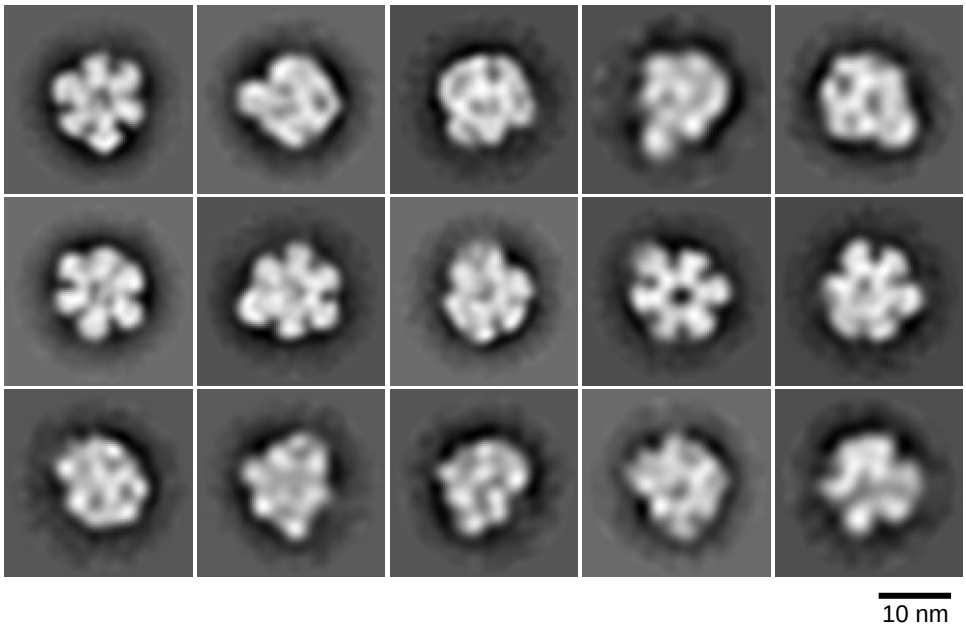

FIG S4 Two-dimensional averaged images of globular complex in F6.
Fifteen classes of clear particle images from 50 classes are represented.

Supplementary figure 5

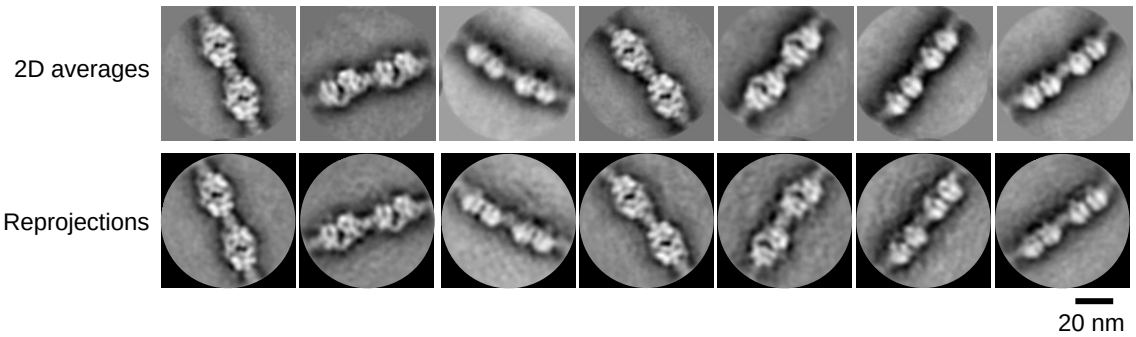

FIG S5 Reprojection images of chain. Two-dimensional averaged images (upper) and the corresponding reprojection images (lower) calculated from the 3D map of the chain are compared.

Movie S1

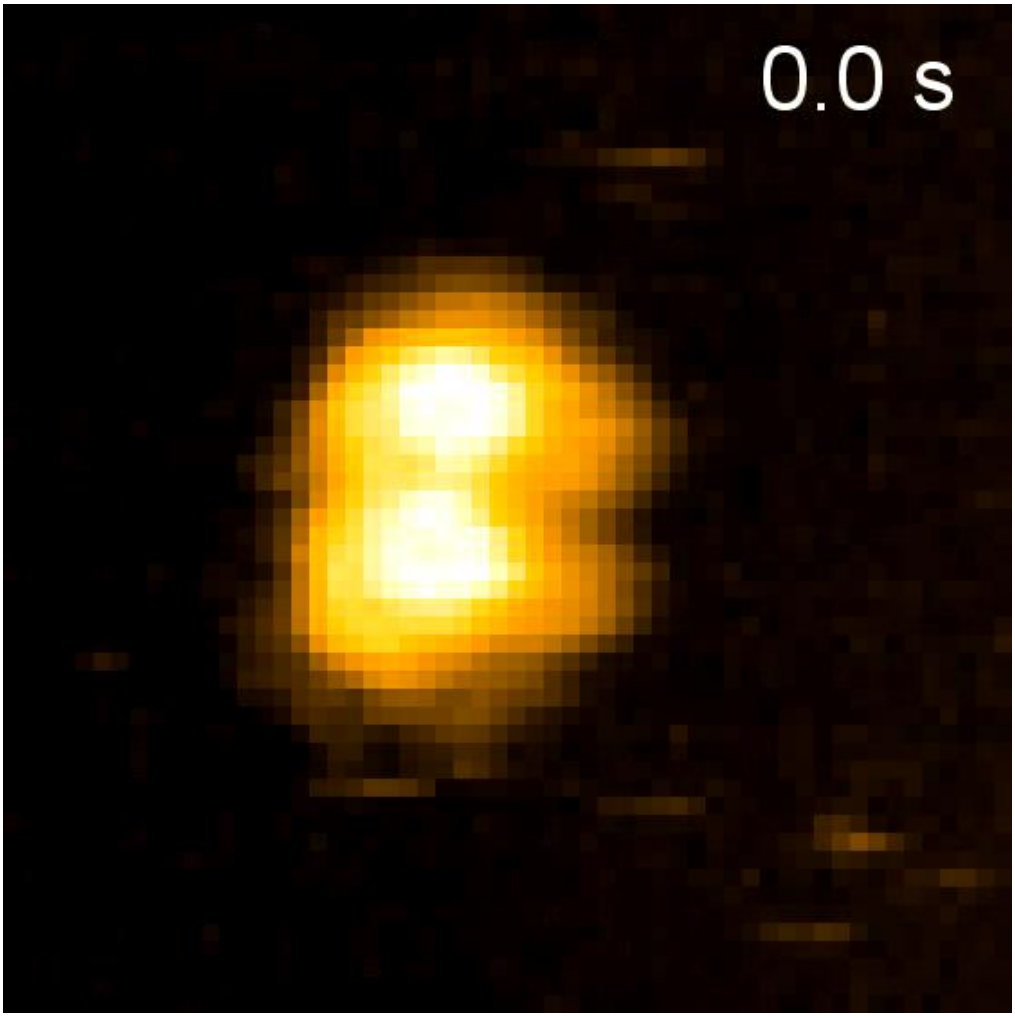

Movie S1 HS-AFM movie showing pattern I particles The particles were scanned at 10 fps. The scanning field was 70 × 70 nm^2 with 56 × 56 pixels. The video was played at 10 fps.

Movie S2

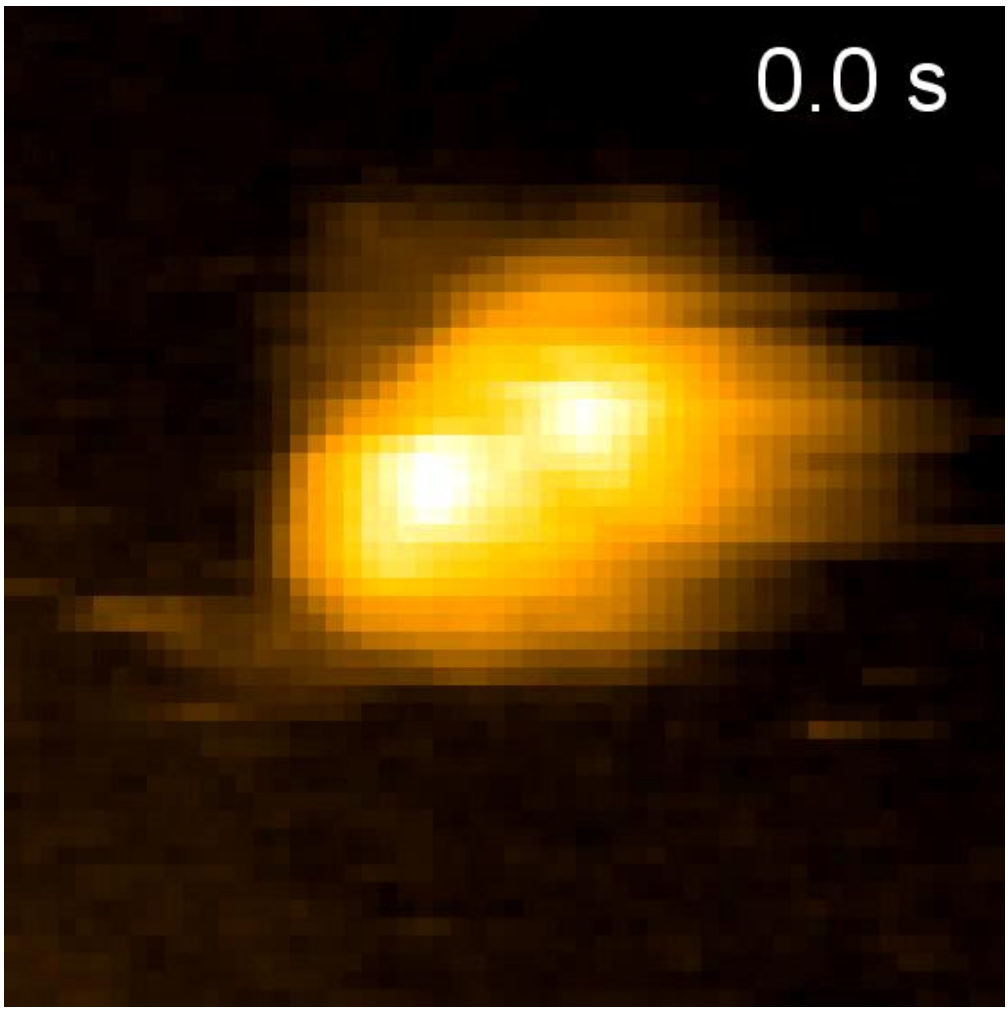

Movie S2 HS-AFM movie showing pattern II particles The particles were scanned at 10 fps. The scanning field was 70 × 70 nm^2 with 56 × 56 pixels. The video was played at 10 fps.

Movie S3

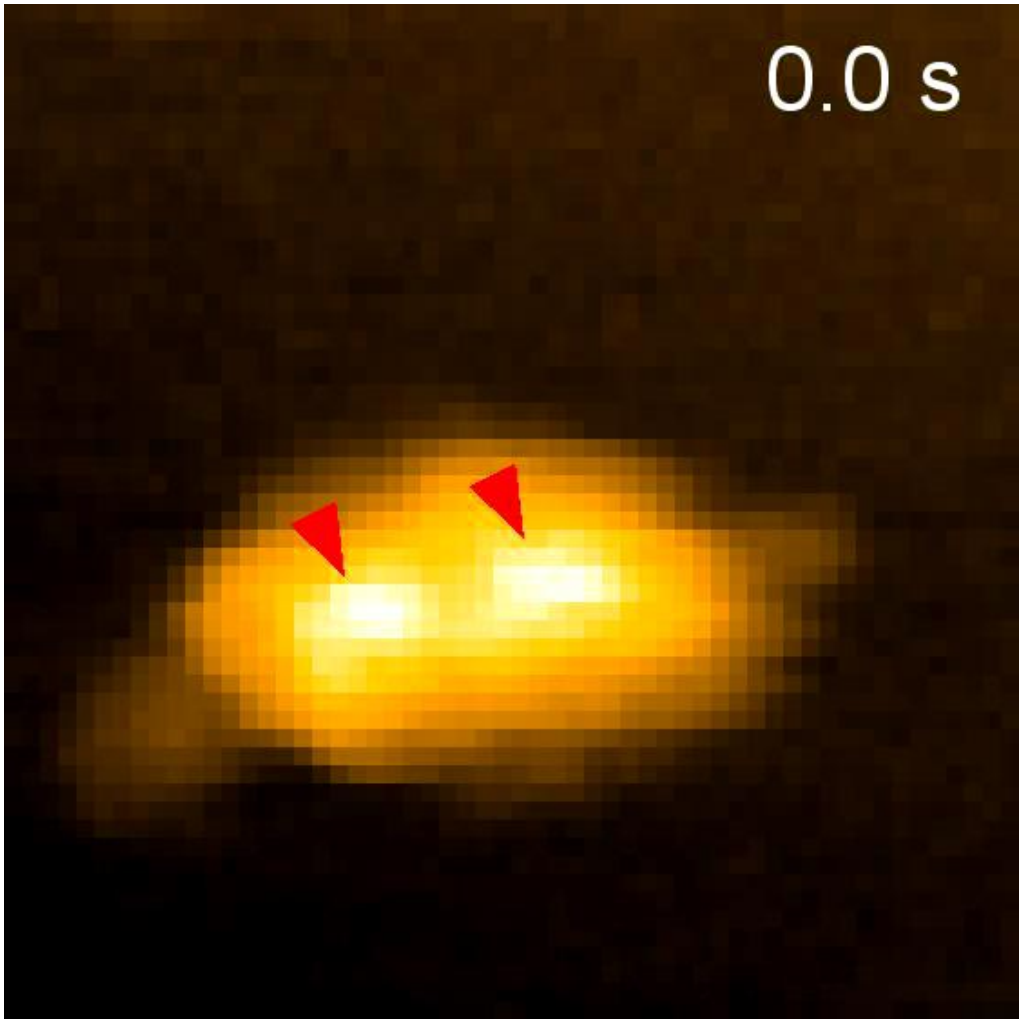

Movie S3 HS-AFM movie showing the shedding process of the peaks. The particles were scanned at 10 fps. The scanning field was 70 × 70 nm^2 with 56 × 56 pixels. The video was played at 10 fps. The peaks are indicated by the red triangles.

Movie S4

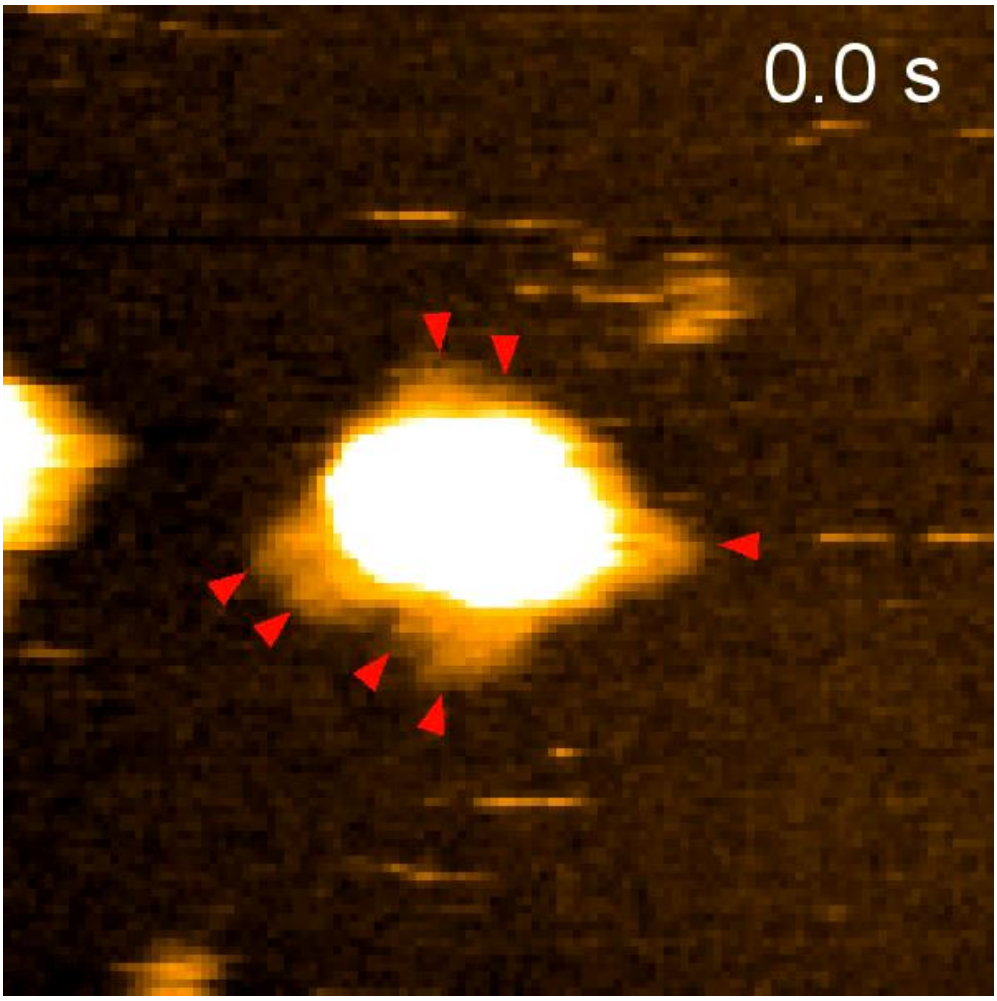

Movie S4 HS-AFM movie showing fluctuations in protrusions. The particles were scanned at 2 fps. The scanning field was 120 × 120 nm^2 with 120 × 120 pixels. The video was played at 1 fps. The protrusions are indicated by the red triangles.